

1 **Petrogenesis and tectonic setting of late Paleoproterozoic diorites in the**

2 **Trans-North China Orogen**

3

4 Zhiyi Wang ^{a, b}, Jun He ^{a*}, Wolfgang Siebel ^b, Shuhao Tang ^a, Yiru Ji ^a, Jianfeng He ^a, Fukun Chen ^a

5

6

7 a: State Key Laboratory of Lithospheric and Environmental Coevolution, School of Earth and

8

Space Sciences, University of Science and Technology of China, Hefei 230026, China

9

b: Institute of Earth and Environmental Sciences, Albert-Ludwig University Freiburg, Freiburg

10

79104, Germany

11

12

13 *Corresponding author: jhe1989@ustc.edu.cn (J. He)

14

15

16 **Abstract:** Unravelling the tectonic setting and evolution of cratons during the late
17 Paleoproterozoic has long been a major focus of geological research. As one of
18 Earth's major cratonic blocks, the North China Craton (NCC) preserves extensive
19 magmatism during this period. Recent investigations have identified numerous 1.78
20 Ga dioritic intrusions along the southern margin and the center of the NCC. The NCC
21 experienced widespread magmatism at ~1.78 Ga, and the tectonic setting of this
22 period remains unclear and needs better understanding. Diorites of the NCC can help
23 to constrain the late Paleoproterozoic tectonic setting in this region. In this paper we
24 report zircon U-Pb ages of ~1.78 Ga and geochemical data of the Jiguanshan diorite.
25 The diorites in the Trans-North China Orogen and the southern margin of the NCC,
26 including the Jiguanshan diorite, have similar element and isotopic characteristics.
27 The average initial $^{87}\text{Sr}/^{86}\text{Sr}$ and $\epsilon_{\text{Nd}}(t)$ values are 0.7052 ± 0.0003 and -6.5 ± 0.2 ,
28 respectively. The initial Pb isotope compositions of the diorite samples do not show
29 significant enrichment of radiogenic lead. In terms of Sr-Nd-Pb isotope compositions
30 and Nb/Ta, Ba/Th, and Sr/Th ratios, the diorites differ from the coeval Xiong'er
31 volcanic rocks and mafic dike swarms. Our results suggest that the diorites originated
32 from basaltic lower crust, rather than from enriched subcontinental lithospheric
33 mantle. Whole-rock and zircon trace element tectonic diagrams indicate that the
34 diorites formed in a rift-related environment. The formation of the diorites indicates a
35 potential transition from late Paleoproterozoic orogenic-related magmatism towards
36 intraplate magmatism.

37 **Key words:** Late Paleoproterozoic, North China, Diorite, Zircon, Sr-Nd-Pb isotopes

39 **1 Introduction**

40 Research on the evolution of the North China Craton (NCC) provides critical insights
41 into Precambrian geological processes (e.g., [Geng et al., 2012](#); [Liu et al., 1992](#)). The
42 NCC was stabilized by the collision and amalgamation of several continental blocks
43 in the late Paleoproterozoic ([Fig. 1a](#); e.g., [Zhao and Zhai, 2013](#); [Zhao et al., 2000a, b](#)).
44 Subsequent widespread magmatic activity across the NCC records the cratonization
45 process, providing critical insights into its stabilization and maturation (e.g., [Zhai,](#)
46 [2011](#)). The petrogenesis of the Paleoproterozoic magmatic rocks preserves key
47 information about regional tectonic evolution and has been linked to the assembly or
48 breakup of the Columbia supercontinent (e.g., [Peng et al., 2007, 2008](#); [Zhao et al.,](#)
49 [2009](#)). Among these events, the ~1.78 Ga magmatic event is particularly distinctive
50 due to its large scale, leading to the production of numerous rock types including the
51 Xiong'er Group, A-type granites and mafic dykes (e.g., [Cui et al., 2010](#); [Hu et al.,](#)
52 [2010](#); [Peng et al., 2007, 2008](#); [Wang et al., 2004](#); [Wang et al., 2014](#)). These rocks are
53 extensively distributed across both the southern margin and Trans-North China
54 Orogen of the NCC. However, the petrogenesis and tectonic setting of these rocks is
55 controversially debated, which revolves around post-collisional/orogenic extension
56 (e.g., [Wang et al., 2004, 2008, 2014](#)), continental arc magmatism (e.g., [He et al., 2009](#);
57 [Zhao et al., 2009](#)), rifting (e.g., [Cui et al., 2010](#); [Zhao et al., 2007](#)), and the
58 involvement of mantle plumes (e.g., [Hou et al., 2008](#); [Peng et al., 2007, 2008](#)).
59 Clarifying the tectonic setting during this period is essential for understanding the
60 geological evolution that followed the late Paleoproterozoic amalgamation of the

61 NCC.

62 In recent years, numerous diorites with ages of *c.* 1780 Ma along the southern margin
63 of the NCC and Shanxi region (Fig. 1b) have attracted significant attention,
64 potentially offering new perspectives for understanding the tectonic evolution of the
65 craton during the late Paleoproterozoic. These rocks include diorites intruding into
66 Xushan Formation (at *c.* 1789 Ma; Zhao et al., 2004), East-West Group dykes (*c.* 1780
67 Ma; Peng et al., 2007), Shizhaigou diorite (*c.* 1780 Ma; Cui et al., 2011), Wafang
68 diorite (*c.* 1750 Ma; Wang et al., 2016), Gushicun diorite (*c.* 1780 Ma; Ma et al.,
69 2023a), Muzhijie diorite (*c.* 1780 Ma; Ma et al., 2023b), Fudian diorite (*c.* 1780 Ma;
70 Ma et al., 2023b), and Jiguanshan diorite (*c.* 1780 Ma; this study). The diorites are
71 widely distributed in an approximate east-west trending belt and possess similar
72 zircon ages. Peng et al. (2007) and Cui et al. (2011) proposed that some of them share
73 identical mantle source regions with the Xiong'er Group volcanic rocks or dyke
74 swarms. Other authors interpret some of them resulting from fractional crystallization
75 (Ma et al., 2023a, b) or from crustal melting with limited mantle influence (Wang et
76 al., 2016). Systematic research of their genesis is crucial for clarifying their formation
77 and constraining the regional geological evolution.

78 The present study focuses on the Jiguanshan diorite and other diorites with ages
79 between 1.78 and 1.75 Ga from the NCC. These diorites have similar geochemical
80 characteristics, suggesting their formation during a single magmatic episode. By
81 evaluating whole rock geochemical and Sr-Nd-Pb isotopic compositions, as well as
82 Hf isotopic compositions of zircons, a better understanding of the tectonic

83 environment and evolution of the NCC during the late Paleoproterozoic is provided.

84

85 **2 Geological background and sample description**

86 The NCC records geological evolution since 3.8 Ga ago (e.g., [Geng et al., 2012](#); [Liu](#)

87 [et al., 1992](#)). It consists of an Archean to Paleoproterozoic metamorphic basement

88 lithologies overlain by Mesoproterozoic unmetamorphosed sedimentary cover (e.g.,

89 [Lu et al., 2008](#); [Zhao and Zhai, 2013](#)). The crystalline basement is composed of several

90 microcontinental blocks ([Fig. 1a](#); [Zhao et al., 2005](#)). Between 1.95 and 1.92 Ga, the

91 Yinshan and Ordos blocks collided along the Khondalite belt to form the Western

92 Block (e.g., [Li et al., 2011](#); [Lu et al., 2008](#); [Zhao et al., 2005](#)). Around 1.9 Ga, the

93 Longgang and Nangrim blocks amalgamated along the Jiao-Liao-Ji belt, forming the

94 Eastern Block (e.g., [Luo et al., 2004](#); [Zhao et al., 2005](#)). The NCC ultimately formed

95 by the assembly of the Eastern and Western Blocks along the central orogenic belt at c.

96 1.85 Ga (e.g., [Zhao and Zhai, 2013](#); [Zhao et al., 2000a, b, 2005](#)). The southern margin

97 of the NCC is separated from the North Qinling Orogen by the Luonan-Luanchuan

98 Fault ([Fig. 1b](#)). Prior to the Mesozoic, the southern margin of the NCC has been the

99 locus of tectonic activity. Therefore, this region is outstanding for studying the

100 Precambrian geological evolution (e.g., [Zhai, 2010](#)).

101 The study area is located within the eastern part of the southern margin of the NCC

102 ([Fig. 1b](#)). The most frequent rocks in this area are metamorphic basement rocks of the

103 Archean Taihua Group. The Taihua Group extends in an east-west direction from

104 Lantian in the west to Wuyang in the east (e.g., [Diwu et al., 2014, 2018](#); [Wang et al.,](#)

105 2020). It is primarily composed of medium- to high-grade metamorphic rocks and has
106 been divided into the Lower and Upper Taihua Complex (e.g., Kröner et al., 1988;
107 Shen, 1994; Wan et al., 2006; Xue et al., 1995; Zhang et al., 1985). The Lower Taihua
108 Complex is dominated by metamorphic mafic rocks and TTG gneisses (e.g., Kröner et
109 al., 1988; Zhang et al., 1985), whereas the Upper Taihua Complex is characterized by
110 supracrustal sequences and metamorphic mafic rocks (e.g., Wan et al., 2006; Xue et
111 al., 1995). Rocks of the Taihua Group record two significant stages of Archean crustal
112 growth (e.g., Diwu et al., 2014, 2018). During the late Paleoproterozoic (1.97–1.80
113 Ga), the Taihua Group underwent widespread amphibolite to granulite facies
114 metamorphism and intense deformation, reflecting collisional processes in the NCC
115 (e.g., Diwu et al., 2018; Sun et al., 2017).

116 The upper part of the basement contains 1780-million-year-old volcanic rocks of the
117 Xiong'er Group (e.g., Zhao et al., 2004, 2007). The Xiong'er volcanic rocks consist
118 mainly of basalts and andesites that are widely distributed along the southern margin
119 of the NCC, and extend as far north as Taiyuan City in Shanxi Province (Zhao et al.,
120 2007). The Xiong'er Group represents the largest magmatic unit of the NCC since the
121 Neoarchean period. At the same time, a large mafic dyke swarm intruded into the
122 NCC. These mafic rocks are interpreted as products of crustal extension during the
123 Colombia supercontinent era (e.g., Hou et al., 2008; Peng et al., 2008).

124 During fieldwork, seven diorite samples were collected from the Jiguanshan diorite on
125 the eastern side of the Jiguanshan hill (or the Jiguan Mountain), about 30 km south of
126 Ruyang County, Henan Province (Fig. 1c and Table S1). The Jiguanshan diorite forms

127 several east-west striking bodies that are cut by the Mesozoic Taishanmiao A-type
128 granite to the west. The Taishanmiao intrusion covers an area of *c.* 290 km² (e.g., He
129 et al., 2021). The northern and eastern part of the Taishanmiao intrusion penetrates the
130 volcanic rocks of the Xiong'er Group (Fig. 1c).

131 The collected rock samples of the Jiguanshan diorite are fresh and greyish with
132 massive textures (Fig. 2a). They are fine-grained with a grain sizes between 0.1–2 mm
133 (Fig. 2b). The main mineral is plagioclase (~60 vol.%), with lamellar and euhedral
134 shape and variable grain size. Under the microscope, the partially sericitized crystals
135 show simple contact twinning and polysynthetic twinning. Some plagioclase crystals
136 show zonal and resorption textures (Figs. 2c-e) and Carlsbad-albite twinning (Fig. 2d).
137 Clinopyroxene (~15 vol.%) formed earlier than plagioclase. Most of the
138 clinopyroxenes have zonal texture (Fig. 2f). Euhedral opaque minerals (~3 vol.%),
139 such as ilmenite, are often enclosed in clinopyroxene. Alkali-feldspar (~10 vol.%)
140 shows hypidiomorphic to xenomorphic texture with imprints of kaolinization (Figs.
141 2c, e). The mineral occurs as K-feldspar and perthite. Quartz (~5 vol.%) occurs as an
142 anhedral crystal. Biotite (~3 vol.%) shows xenomorphic texture or is altered into
143 chloride (Figs. 2c, e). In addition, accessory minerals such as zircon and ilmenite
144 account for about 3 vol.% (Fig. 2f).

145

146 **3 Analytical methods**

147 **Whole rock major and trace elements:** Seven representative fresh rock samples

148 were grinded into powders to less than 200 mesh size. Major element composition of
149 whole-rock samples was analyzed by X-ray fluorescence (XRF) at ALS Chemex
150 (Guangzhou) by using PANalytical PW2424 instrument. Trace element concentrations
151 were determined using Agilent 7700 inductively coupled plasma mass spectrometry
152 (ICP-MS) at the University of Science and Technology of China (USTC). Measured
153 concentrations of the reference materials (GSR-1, BCR-2, and AGV-2) are within 10%
154 of their recommended values and the analytical uncertainties are better than 5%.

155 **Whole-rock Sr-Nd-Pb isotopes:** Whole-rock Sr-Nd-Pb isotope analysis was
156 performed in the Laboratory of Radiogenic Isotope Geochemistry, USTC. C. 100 mg
157 whole-rock powders were decomposed in purified HF and HNO₃ acid solution for Pb
158 isotopic analysis and purified HF and HClO₄ acid solution for Sr-Nd isotopic analysis.
159 Sr and Nd were separated by an AG 50W-X12 resin (200–400 mesh size) and purified
160 using the Sr-Spec® ion-exchange resin for Sr and LN-Spec® resin for Nd. All isotopic
161 measurements were measured on a Triton Plus mass spectrometer of Thermo
162 Scientific™. Sr and Nd ratios were normalized to ⁸⁶Sr/⁸⁸Sr = 0.1194 and ¹⁴³Nd/¹⁴⁴Nd
163 = 0.7219, respectively. Pb isotope ratios were corrected for mass fractionation using a
164 fractionation factor of 0.1% per atomic mass unit based on repeated measurements of
165 reference material NIST NBS 981 (Wang et al., 2023b). Total procedure blanks for Sr,
166 Nd, and Pb were less than 200 pg. Detailed analytical procedures were described in
167 Chen et al. (2000, 2007). Errors for the initial Sr and Nd isotope ratios were obtained
168 by the error transfer formula, which is shown in Table 2 for Sr and Table 3 for Nd.
169 Detailed formulas can be found in Siebel et al. (2005). A 5% age error, a 2‰ ⁸⁷Rb/⁸⁶Sr

170 measurement error, and a 0.3‰ $^{87}\text{Sr}/^{86}\text{Sr}$ measurement error were used as
171 uncertainties for the initial Sr value calculation. A 5% age error, a 0.3‰ $^{147}\text{Sm}/^{143}\text{Nd}$
172 error, and the $^{143}\text{Nd}/^{144}\text{Nd}$ measurement error were used for calculating the initial Nd
173 isotope uncertainty.

174 **Zircon U-Pb geochronology and trace element composition:** Zircon crystals were
175 separated from the rock samples by standard mineral separation procedures. Grains
176 with intact crystal shape and no obvious inclusions were selected and embedded in
177 epoxy resin under a binocular microscope. Most of the zircon gains were polished to
178 half to two thirds of their original thickness and then cleaned in ultra-pure water by
179 ultrasonic waves. Cathodoluminescence (CL) image analysis was done on a scanning
180 electron microscope (SEM) at the USTC. Zircon U-Pb isotopic and trace element
181 compositions were obtained by laser-ablation inductively-coupled plasma mass
182 spectrometry (LA-ICP-MS) at the USTC. The beam spot diameter was 32 μm ,
183 operating at a repetition rate of 10 Hz. Helium served as the carrier gas. Zircon 91500
184 was used as a standard for age calculation. The NIST SRM 610 and 612 were utilized
185 as reference materials for element content adjustment. U-Pb ratios and uranium and
186 lead concentration data were calculated by the ICPMSDataCal software ([Liu et al.,](#)
187 [2010](#)). Concordia and weighted mean age plots were made using IsoplotR ([Vermeesch,](#)
188 [2018](#)).

189

190 **4 Analytical results**

191 Whole-rock compositions of the Jiguanshan diorite are given in [Table 1](#), and
192 Sr-Nd-Pb isotope compositions and error calculations are shown in [Tables 2 to 4](#). Age
193 results of zircon grains from four samples are given in [Table S1](#), zircon trace element
194 composition in [Table S2](#).

195

196 **4.1 Zircon U–Pb isotopic ages**

197 Zircon grains from the Jiguanshan diorite are transparent to pale yellow with
198 subhedral to euhedral habitus. They measure *c.* 100–300 µm in length and have aspect
199 ratios between 1:1 and 3:1. Most of them show oscillatory zoning in the CL images
200 ([Fig. 3](#)), which suggests a magmatic origin.

201 Twenty-nine zircon grains from sample ZY2202 yield $^{207}\text{Pb}/^{206}\text{Pb}$ ages varying from
202 1885 ± 44 Ma to 1643 ± 42 Ma giving a weighted mean age of 1772 ± 16 Ma (2σ , $n=29$,
203 $\text{MSWD}=2.2$, [Fig. 4a](#)). Thirty-two zircon grains from sample ZY2204 yield $^{207}\text{Pb}/^{206}\text{Pb}$
204 ages varying from 1902 ± 54 Ma to 1635 ± 47 Ma with a weighted mean age of 1742
205 ± 15 Ma (2σ , $n=32$, $\text{MSWD}=1.6$, [Fig. 4b](#)). Twenty-six out of twenty-seven zircon
206 grains from sample ZY2205 yield $^{207}\text{Pb}/^{206}\text{Pb}$ ages varying from 1933 ± 52 Ma to
207 1692 ± 44 Ma and a weighted mean age of 1760 ± 18 Ma (2σ , $n=26$, $\text{MSWD}=0.66$, [Fig.](#)
208 [4c](#)). One zircon with a $^{207}\text{Pb}/^{206}\text{Pb}$ age of 1639 ± 46 Ma (96% concordance) was
209 excluded from the calculation after being identified as a statistical outlier by the
210 IsoplotR program ([Fig. 4c](#)). The limited number of zircon grains of this age precludes
211 a robust geological interpretation. Thirty zircon grains of sample ZY2207 yield

212 $^{207}\text{Pb}/^{206}\text{Pb}$ ages ranging from 1900 ± 54 Ma to 1700 ± 36 Ma with a weighted mean
213 age of 1771 ± 17 Ma (2σ , $n=30$, MSWD=1, [Fig. 4d](#)).

214 Most zircon grains have Th/U ratios >1 , supporting their magmatic origin ([Table S1](#)).
215 Some grains deviate from the Concordia curve, which is related to lead loss events or
216 radiation damage ([Fig. 4a-d](#)). The weighted mean age of the Jiguanshan diorite of *c.*
217 1780 Ma suggests that the diorite body formed in the late Paleoproterozoic.

218

219 **4.2 Whole-rock geochemical composition**

220 SiO₂ contents of the Jiguanshan diorite vary between 55.57 and 59.44 wt. % and the
221 sum of K₂O+Na₂O from 5.57 to 6.03 wt. %, corresponding to gabbroic diorite to
222 diorite composition according to the TAS diagram ([Fig. 5a](#)). K₂O contents range from
223 2.97 to 3.21 wt. % and fall within the high-K calc-alkaline fields ([Fig. 5b](#)). The
224 samples from the Jiguanshan diorite have consistent A/CNK ratios ranging from 0.78
225 to 0.81 and A/NK >1 , which classify them as metaluminous rocks ([Fig. 5c](#)). Mg[#]
226 ($\text{Mg}^{\#} = (\text{MgO} + \text{FeO}_{\text{total}})/\text{MgO} \times 100$) values range from 34 to 39 ([Fig. 5d](#)).

227 The Jiguanshan diorite depicts enrichment in large ion lithophile elements (LILE),
228 such as Rb, Ba, and K, and negative anomalies of Sr, Ti, Nb, and Ta ([Fig. 6a](#)). ΣREE
229 contents range from 361 to 393 ppm. Light rare earth elements (LREE) exhibit
230 stronger enrichment, while heavy rare earth elements (HREE) are relatively depleted
231 ([Fig. 6b](#)). (La/Yb)_N ratios range from 12.2 to 15.0 (subscript N denotes normalization
232 against chondrite La and Yb contents) with Eu/Eu^{*} (Eu/Eu^{*} = $2\text{Eu}_N/(\text{Sm}_N + \text{Gd}_N)$,

233 subscript N denotes normalization against chondrite Sm and Gd contents) ratios
234 ranging from 0.57 to 0.68 (Table 1).

235

236 **4.3 Whole-rock Sr-Nd-Pb isotope compositions**

237 All initial radiogenic isotope values and the errors of the initial Sr, Nd and Pb isotope
238 ratios reported herein are calculated back to an age of 1780 Ma. The measured
239 $^{87}\text{Sr}/^{86}\text{Sr}$ ratios for the Jiguanshan diorites vary from 0.715177 ± 0.000011 to 0.724714
240 ± 0.000012 (2σ). Initial Sr ratios range from 0.7020 ± 0.0007 to 0.7058 ± 0.0010 (2σ ,
241 Fig. 7a). Measured $^{143}\text{Nd}/^{144}\text{Nd}$ values vary from 0.511129 ± 0.000008 to 0.511329
242 ± 0.000007 (2σ). Initial $^{143}\text{Nd}/^{144}\text{Nd}$ isotope compositions range from 0.509924
243 ± 0.000061 to 0.510090 ± 0.000063 (2σ), corresponding to initial ε_{Nd} values of -8.04
244 ± 1.20 to -4.80 ± 1.23 (2σ , Fig. 7b) and two-stage Nd model ages (T_{DM2}) of 2.94 Ga to
245 2.68 Ga. Pb isotopic compositions are as follows: $^{206}\text{Pb}/^{204}\text{Pb} = 15.832\text{--}16.167$,
246 $^{207}\text{Pb}/^{204}\text{Pb} = 15.170\text{--}15.243$, and $^{208}\text{Pb}/^{204}\text{Pb} = 36.046\text{--}37.324$. Initial Pb isotope
247 ratios are significantly lower: $^{206}\text{Pb}/^{204}\text{Pb}_i$ ratios ranging from 14.965 to 15.295,
248 $^{207}\text{Pb}/^{204}\text{Pb}_i$ ratios ranging from 15.090 to 15.150, $^{208}\text{Pb}/^{204}\text{Pb}_i$ ratios ranging from
249 34.398 to 35.825, with $^{238}\text{U}/^{204}\text{Pb}$ and $^{232}\text{Th}/^{238}\text{U}$ ratios ranging from 2.3 to 2.9 and
250 5.3 to 7.8, respectively (Fig. 8).

251

252 **5 Discussion**

253 **5.1 Compositional characteristics of late-Paleoproterozoic diorites of the NCC**

254 On a regional scale, the late Paleoproterozoic diorites of the NCC are distributed in a
255 roughly east to west direction, unlike the north-northwest (NNW) strike direction, that
256 characterizes the contemporaneous mafic dykes (Hou et al., 2008; Peng et al., 2007,
257 2008). Intrusion ages of the diorites are concentrated between 1780 and 1750 Ma. All
258 diorites have similar geochemical and isotopic compositions and can be regarded as a
259 compositional homogeneous rock group.

260 Most of the late-Paleoproterozoic diorites of the NCC have silica contents in the range
261 of 52-62 wt. % (Fig. 5a). Total alkali content (K_2O+Na_2O) of 5-7 wt. % suggests a
262 subalkaline character (Fig. 5a). K_2O contents range from 2-5 wt. % in accordance
263 with a high-K calc-alkaline to shoshonite composition (Fig. 5b). The ASI and $Mg^{\#}$
264 values of the samples, except for a few data points that deviate significantly, are
265 mostly homogeneous, with weighted average values of 0.81 and 37, respectively (Figs.
266 5c, d). In primitive mantle normalization multi-element diagrams, all diorites display
267 enrichment of LILEs, such as Rb, Ba, and K, and depletion of high field strength
268 elements (HFSEs), such as Na, Ta, Th, U, and Ti (Fig. 6). On the rare earth element
269 normalization diagrams, they display negative Eu anomalies with enrichment in
270 LREEs and flat distribution of HREEs (Fig. 6).

271 All diorites have similar Nd isotopic compositions with a mean initial ϵ_{Nd} value of
272 -6.5 ± 0.2 (2σ , $n=41$, Fig. 7b), when calculate back to 1780 Ma (Table 3). The overall
273 range of initial ϵ_{Nd} values is from -10.2 ± 1.2 to -4.8 ± 1.2 (2σ , Fig. 7b). Some samples
274 from the Wafang diorite (or Muzhijie diorite, Ma et al, 2023b; Wang et al, 2016) have
275 enriched Nd isotope composition, which can be explained by assimilation or

276 contamination of continental crust due to their higher zirconium content (Fig. 7b;
277 Table 3). Overall, the initial ϵ_{Nd} values and the corresponding two-stage Nd model
278 ages (T_{DM2}) of the diorites are consistent with each other except for the Wafang diorite
279 (Table 3).

280 Initial ϵ_{Hf} values of zircons from the diorites in the NCC show a wide but consistent
281 range of variations, i.e., from -17 to -2.5 in the Gushicun diorite (Ma et al., 2023a; Fig.
282 7c), from -14 to 0.55 in the Muzhijie diorite (Ma et al., 2023b; Fig. 7c), and from -17
283 to 0.95 in the Fudian diorite (Ma et al., 2023b; Fig. 7c). The diorites have similar
284 Nd-Hf isotopic compositions and form a coherent group in geochemical diagrams,
285 indicating a close genetic relationship.

286

287 **5.2 Initial Sr isotope composition and magma source characteristics**

288 The late Paleoproterozoic diorites of the NCC show a large range in whole-rock initial
289 Sr isotope composition (Fig. 7a; Jiguanshan diorite: 0.7020 to 0.7058; Wafang diorite:
290 0.7004 to 0.7050; Shizhaigou diorite: 0.7005 to 0.7053; East-West group dikes:
291 0.7011 to 0.7053). Determining magma sources for rocks with widely varying initial
292 Sr ratios is complex, as Sr isotopes can be affected by magma mixing, assimilation,
293 contamination, and melting degrees (e.g., Gao et al., 2015; Wolf et al., 2019; Zeng et
294 al., 2005).

295 The whole-rock Nd and Sr isotope composition of the diorites suggest a
296 heterogeneous magma source (Fig. 7d). It might be argued that this could be the effect

297 of mixing between crustal and mantle sources. However, mantle-derived rocks often
298 have high MgO contents and elevated compatible element concentrations such as Ni
299 and Cr, which is inconsistent with the element characteristics of the diorites (Table 1,
300 see previous references). Variability in Sr isotope ratios can result from different
301 degrees of source melting. However, a mica- and feldspar-rich source with high Rb/Sr
302 ratios can produce melts with more radiogenic $^{87}\text{Sr}/^{86}\text{Sr}$ ratios (e.g., [Hu et al., 2018](#)).
303 Melts affected by dehydration of amphibole typically have low $^{87}\text{Sr}/^{86}\text{Sr}$ ratios and
304 adakitic characteristics (e.g., [Rapp and Watson, 1995](#); [Wolf et al., 1993](#)). Thus,
305 different degrees of source melting are unlikely to be the main cause for the isotopic
306 composition of the diorites.

307 Initial $^{87}\text{Sr}/^{86}\text{Sr}$ ratios <0.704 are negatively correlated with the $^{87}\text{Rb}/^{86}\text{Sr}$ ratios ([Fig.](#)
308 [7a](#)). For initial $^{87}\text{Sr}/^{86}\text{Sr}$ ratios >0.704 , such correlation does no longer exist. A reason
309 for this could be the large uncertainty propagation of the initial whole-rock Sr isotope
310 ratios especially for old samples. Among all diorites there are samples with initial
311 $^{87}\text{Sr}/^{86}\text{Sr}$ ratios >0.704 . Excluding outliers, the mean average initial $^{87}\text{Sr}/^{86}\text{Sr}$ ratio is
312 0.7052 ± 0.0003 (2σ , $n=8$), which might represent the most likely initial Sr isotope
313 composition of the magma source ([Fig. 7a](#)).

314 The initial Sr ratios of the Xiong'er Group rocks vary widely and tend to be more
315 radiogenic compared to the diorites ([Fig. 7d](#)). The initial Sr ratios of the diorites are
316 more similar to lower crustal Archean xenoliths from the southeastern NCC (initial
317 $^{87}\text{Sr}/^{86}\text{Sr}$ ratios: $0.7039\text{--}0.7068$, $t=1780$ Ma, e.g., [Huang et al., 2004](#)), suggesting that
318 they are more likely associated with lower crustal rocks of the NCC rather than an

319 enriched mantle source like the volcanic rocks of the Xiong'er Group.

320

321 **5.3 Petrogenesis of the dioritic rocks**

322 Several models have been proposed for the petrogenesis of intermediate dioritic rocks
323 including partial melting of metasomatized mantle (e.g., [Chen et al., 2021](#)), partial
324 melting of subducted oceanic crust and subsequent melt-peridotite reaction (e.g.,
325 [Kelemen, 1995](#); [Stern and Kilian, 1996](#)), magma mixing/mingling (e.g., [Reubi and](#)
326 [Blundy, 2009](#); [Streck et al., 2007](#)), melting of basaltic rocks (e.g., [Jackson et al., 2003](#);
327 [Petford and Atherton, 1996](#)), as well as fractional crystallization of basaltic magmas
328 (e.g., [Castillo et al., 1999](#)).

329 The diorites from the NCC have low compatible element concentrations, suggesting
330 that they were not derived directly from a mantle source ([Fig. 9a](#)). Larger contribution
331 of mantle material can also be excluded due to their initial Nd isotope features ([Fig.](#)
332 [7b](#)), silica and Mg[#] values ([Fig. 5d](#)).

333 Partial melting of subducting oceanic crust can also form rocks of intermediate
334 composition, such as adakites, which often exhibit high Sr/Y ratios (>20) and low Y
335 contents (<18 ppm) (e.g., [Defant and Drummond, 1990](#); [Peacock et al., 1994](#)). The
336 Jiguanshan and other diorites from the NCC have relatively high Y and Sr contents
337 with Sr/Y ratios <15. Thus, partial melting of oceanic crust does not appear to have
338 played a role during the genesis of the diorites.

339 Cr contents decrease with decreasing MgO, indicating fractionation of clinopyroxene

340 (Fig. 9a). CaO contents decrease with increasing SiO₂, suggesting crystallization of
341 minerals, such as plagioclase or clinopyroxene (Fig. 9b). However, Al₂O₃ and Na₂O
342 contents do not significantly decrease with increasing SiO₂, indicating that plagioclase
343 and clinopyroxene were not significant fractionation phases (Figs. 9c-d). The increase
344 in K₂O contents with increasing SiO₂ suggests no biotite and/or K-feldspar
345 fractionation during magmatic evolution (Fig. 9e). Increasing SiO₂ and decreasing
346 TiO₂ indicate crystallization and fractionation of Ti-bearing minerals, such as ilmenite
347 (Fig. 9f). Eu/Eu^{*} values of the diorites do not show significant changes with Sr
348 contents, which provides evidence that fractionation of plagioclase from the melt was
349 not significant (Fig. 9g).

350 From the above discussion, it can be concluded that the petrogenesis of the diorites in
351 the NCC was associated with minor fractional crystallization processes. Whole-rock
352 La/Yb versus La and Zr/Sm versus Zr correlations are as expected for a partial
353 melting process (Figs. 9h-i). This implies that the formation of the diorites may be
354 closely related to the partial melting of a basaltic protolith.

355 Basement rocks of the lower Taihua Group at the southern margin of the NCC consist
356 of amphibolite (e.g., Diwu et al., 2014, 2018; Wang et al., 2020). Partial melting of
357 amphibolite can lead to the production of intermediate to acidic magmas (e.g., Beard
358 and Lofgren, 1991; Rapp and Watson, 1995). The amphibolites of the Taihua Group
359 are characterized by low K content and low K₂O/Na₂O ratios (<0.5, Wang et al.,
360 2019), making it difficult to generate high-K₂O rocks. (Beard and Lofgren, 1991;
361 Roberts and Clemens, 1993). Partial melting of amphibolite typically results in the

362 formation of peraluminous melts (e.g., Beard and Lofgren, 1991; Rapp and Watson,
363 1995), whereas the diorites in the NCC have low Al_2O_3 content and metaluminous
364 character (Fig. 5c; Weighted average A/NCK values of 0.81). Additionally, the ε_{Nd}
365 values of the Taihua Group amphibolites at $t=1780$ Ma vary widely from -6.7 to 0.4,
366 different from those of the diorites (Wang et al., 2019). Therefore, it seems unlikely
367 that the diorites formed by the partial melting of Taihua Group amphibolites.

368 Mafic rocks of the Xiong'er Group and mafic dyke swarms were argued to be the
369 source of the diorites (Cui et al., 2011; Ma et al., 2023b; Peng et al., 2007). Such
370 rocks possess a relatively large range of initial Sr and Nd isotopic compositions (Fig.
371 7d), while the initial Nd isotopic compositions of the diorites are relatively
372 homogeneous (Fig. 7b). Whole-rock initial Nd ratios and zircon initial Hf isotope
373 ratios of the Xiong'er Group rocks are also enriched (Fig. 7c). Initial Pb isotopic
374 compositions of the mafic dykes and Xiong'er Group rocks are very radiogenic and
375 variable (Figs. 8a, b), which is due to the high U and Th contents of the protolith,
376 indicating the presence of an enriched subcontinental lithospheric mantle source (e.g.,
377 Hou et al., 2008; Peng et al., 2004, 2007; Wang et al., 2004, 2010; Zhao et al., 2007).
378 Based on the previous discussion, the geochemical characteristics of the diorites are
379 more compatible with a crustal origin and the isotopic compositions of the diorites
380 indicate that they were not derived from an enriched mantle source.

381 Additionally, the Xiong'er volcanic rocks have lower Nb/Ta ratios and Nb contents
382 compared to the diorites (Fig. 10a). Nb and Ta share a similar valence state and
383 atomic radii, but they can undergo fractionation during the subduction process

384 (Jochum et al., 1986; Shannon, 1976). The Xiong'er volcanic rocks, with higher and
385 positively correlated Ba/Th and Sr/Th ratios (Figs. 10a-b), likely originated from a
386 source influenced by an early subduction component, whereas the diorites appear to
387 be less affected by early subduction-related materials. Therefore, it seems likely that
388 the diorites were formed by partial melting of a mafic lower crustal protolith on top of
389 an enriched subcontinental lithospheric mantle beneath the NCC.

390

391 **5.4 Tectonic implications**

392 After Paleoproterozoic collisional and amalgamation, the NCC was intruded by
393 diverse magmatic rocks, which have been interpreted as products of continental arc
394 magmatism, post-collisional extension, or continental rift/mantle plume magmatism.

395 The volcanic rocks of the Xiong'er Group along the southern margin of the NCC are
396 dominated by andesites, exhibiting calc-alkaline characteristics and negative Nb-Ta-Ti
397 anomalies (Jia, 1987; He et al., 2009; Zhao et al., 2009). These signatures together
398 with Nd isotope evidence for ancient crustal assimilation and multiphase volcanic
399 activities, support a continental arc environment for the formation of the Xiong'er
400 Group (He et al., 2009; Zhao et al., 2009).

401 The radially distributed mafic dike swarms, accompanied by A-type granite intrusions
402 and rift-related sedimentary sequences, are indicative of a continental rift setting (e.g.,
403 Fan et al., 2024; Xu et al., 2008; Zhao et al., 2002; Zhao et al., 2002, 2007). The
404 Xiong'er Group is dominated by andesites, dacites, and rhyolites with minor basaltic

405 andesites, which some researchers interpret as an atypical bimodal suite suggestive of
406 a continental rift setting (Zhao et al., 2002, 2007). Furthermore, the 1.80 to 1.75 Ga
407 old mafic dike swarms are distributed in a radial or concentric pattern centered on the
408 Xiong'er Rift and extending northward (Peng et al., 2007). They share geochemical
409 characteristics, such as high TiO₂ and MgO contents, enrichment in LREEs, Ba, and
410 K, and depletion in Nb-Ta which is interpreted as evidence for lithospheric extension
411 induced by mantle plume upwelling (e.g., Hou et al., 2008; Peng et al., 2007, 2008).

412 The post-collisional extension model emphasizes that the late Paleoproterozoic
413 magmatism occurred during lithospheric delamination and possibly slab detachment
414 (e.g., Wang et al., 2004, 2008, 2014, 2023a). The mafic dikes are enriched in LILEs
415 and LREEs but depleted in HFSEs, and show negative $\varepsilon_{\text{Nd}}(t)$ and $\varepsilon_{\text{Hf}}(t)$ values. This
416 suggests derivation from an enriched lithospheric mantle previously metasomatized
417 by subduction zone fluids (e.g., Hu et al., 2010; Wang et al., 2004, 2008, 2014). The
418 dikes are concentrated in the Trans-North China Orogen and nearby areas, consistent
419 with extensional fractures caused by a rising asthenosphere (Wang et al., 2004, 2008,
420 2014). Their geochemical features, lacking OIB or asthenospheric mantle affinities,
421 do not support a mantle plume origin (Wang et al., 2014).

422 Calk-alkaline diorites are important intermediate rock that typically form at island
423 arcs, subduction zones, and continental collision orogenic belts along convergent plate
424 boundaries. Island arc intermediate rocks, such as boninites and andesites are
425 generally characterized by high MgO, Cr, and Ni contents (Hickey et al., 1982; Rapp
426 and Watson, 1995), whereas continental arc intermediate rocks typically show high

427 Al_2O_3 content with a wider range of $^{87}\text{Sr}/^{86}\text{Sr}$ and $^{143}\text{Nd}/^{144}\text{Nd}$ isotope compositions,
428 reflecting an obvious influence of continental crust or more enriched sources
429 (Hawkesworth et al., 1979; Peacock et al., 1994). The Paleoproterozoic diorites of the
430 NCC lack the compositional features of arc-related rocks, meanwhile, their trace
431 element distributions differ from those of island arc and continental arc intermediate
432 rocks. For example, the diorites do not show significant enrichment in Sr, Th, and U
433 such as found in arc-related rocks (Fig. 6a). The diorites also exhibit a negative Eu
434 anomaly in the REE diagram, which is different from arc-related rocks (Fig. 6b).
435 Diorites in collisional orogenic belts have high MgO and K_2O contents and
436 adakite-like characteristics with high Sr/Y and La/Yb ratios (Yang et al., 2015).
437 However, Paleoproterozoic diorites of the NCC do not show typical arc-related
438 element and isotopic signatures, suggesting formation in a non-subduction
439 environment.

440 Diorites can also form during crustal extension (Asmerom et al., 1990; Liu et al.,
441 2024). The NCC was in a post-collisional extensional setting after its final
442 amalgamation (e.g., Zhai, 2010). During this stage, magmatism becomes more
443 complex (Bonin, 2004). Zircon is a very stable mineral and its trace elements offer
444 significant potential for distinguishing between different tectonic settings. For the
445 following discussion, zircon samples with La contents (< 1 ppm) were selected to
446 ensure accurate information from zircon trace element contents without interference
447 from the inclusion of other accessory phases (Zou et al., 2019). All zircons from the
448 diorites plot within the continental area in the U/Yb versus Y diagram (Fig. 11a), and

449 most of them fall into a rift-controlled tectonic environment in tectonic discrimination
450 diagrams (Figs. 11b, c; Carly et al., 2014).

451 Furthermore, HFSE elements, such as Zr, Nb, Ta, Hf, and Th, are important tectonic
452 discriminators. The distinctive Th content in arc magmas is primarily due to its low
453 solubility in subduction zone fluids and its contribution from sedimentary components
454 (e.g., Bailey and Ragnasdottir, 1994; Pearce and Peate, 1995). Arc-related/orogenic
455 magmas usually have less Nb than those of within-plate settings (e.g., Pearce and
456 Peate, 1995; Sun and McDonough, 1989). Nb in zircon is thought to be incorporated
457 through xenotime-type substitution (Schulz et al., 2006) and is suggested to reflect the
458 magma composition with minimal influence of magmatic fractionation (Hoskin et al.,
459 2000; Schulz et al., 2006). In the Nb/Hf versus Th/U and Hf/Th versus Th/Nb
460 diagrams, zircons from the Fudian and Gushicun diorites plot both within or close to
461 the arc-related/orogenic area (Figs. 11d, e). The Jiuganshan and Muzhijie diorites plot
462 both in the arc-related/orogenic and within-plate/anorogenic areas (Figs. 11d, e).
463 Whole-rock Ta/Yb and Th/Yb ratios of the diorites are uniform (Fig. 11f), all falling
464 within the overlapping area of the ACM (active continental margins) and WPVZ
465 (within-plate volcanic zone). This may indicate that the post-collisional extension
466 during this period proceeded continuously and progressively into a rift evolution.
467 Nevertheless, the diorites preserve a record of superposition of components from
468 multiple tectonic settings.

469 After the ~1.85 Ga collisional event, the NCC entered into a prolonged
470 post-collisional extensional stage (Fig. 12). During this stage, magmatism was

471 primarily controlled by crustal thickening and remelting, leading to the widespread
472 formation of various crust-derived granites (e.g., [Geng et al., 2006](#); [Zhao et al., 2008, 2018](#)). Subsequent slab breakoff and gravitational collapse of the thickened crust
473 triggered extension in the mid-upper crust and emplacement of felsic magmas ([Deng et al., 2016a](#); [Wang et al., 2023a](#); [Xu et al., 2024](#)). At *c.* 1.78 Ga, lithospheric thinning
474 induced upwelling of the asthenosphere, causing further partial melting of previously
475 subduction-fluid-metasomatized lithospheric mantle (e.g., [Peng et al., 2007, 2008](#);
476 [Wang et al., 2010, 2014](#); [Zhao et al., 2002, 2007](#)). Following this event, the magmatic
477 activity in this region became dominated by A-type granites and alkaline rocks,
478 marking a transition to an anorogenic intracontinental extensional setting (e.g., [Deng et al., 2016b](#); [Wang et al., 2024](#)). The 1.78 Ga old crust-derived diorites show
479 transitional geochemical features, retaining some remnant effects of orogenic
480 magmatism while gradually evolving toward intraplate magmatism. It reflects the
481 ongoing extension of the NCC after its amalgamation.
482

483

484 6 Conclusions

485
486 The Jiguanshan diorite yields a U-Pb zircon age of *c.* 1.78 Ga. The intrusion displays
487 geochemical features in common with other Paleoproterozoic diorite intrusions of the
488 NCC. The diorite emplaced contemporaneous with the Xiong'er volcanic rocks and
489 the mafic dyke swarms, representing a significant period of magmatism in the NCC.
490

491 The diorites were produced by partial melting of a mafic protolith. The Sr-Nd-Pb-Hf
492 isotopic characteristics indicate that the source was not the same as that for the

493 Xiong'er volcanic rocks or the mafic dyke swarms. Instead, the diorites were likely
494 derived from the lower crust of the NCC.

495 The formation of Paleoproterozoic diorites in the NCC was not connected with arc
496 magmatism. Instead, it was associated with a rift setting. The formation of diorite
497 records the transition of crustal origin rocks from orogenic-related magmatism to
498 intraplate magmatism during the post-collision extensional stage. It therefore reflects
499 the ongoing extension of the NCC after its amalgamation.

500

501

502 **Acknowledgements**

503 This study was financially supported by the Strategic Priority Research Program of
504 the Chinese Academy of Sciences (grant Nos. XDA0430203) and the National
505 Natural Science Foundation of China (grant Nos. 42202069 and 41872049). Zhiyi
506 Wang was financially supported by China Scholarship Council (202306340065). We
507 thank P. Xiao and Z.-H. Hou for assistance during analysis.

508

509 **Author contributions**

510 Zhiyi Wang: Investigation, Writing - Review & Editing; Jun He & Fukun Chen:
511 Supervision, Writing - Review & Editing, Funding acquisition; Wolfgang Siebel:
512 Conceptualization, Writing - Review & Editing; Shuhao Tang, Yiru Ji, Jianfeng He:

513 Data collection for this paper.

514

515 **Conflict of interest:**

516 The authors declare no competing financial and non-financial interests for this study.

517

518

519 **References**

520 Asmerom, Y., Snow, J. K., Holm, D. K., Jacobsen, S. B., Wernicke, B. P., and Lux, D. R.: Rapid uplift
521 and crustal growth in extensional environments: An isotopic study from the Death Valley region,
522 California. *Geology*, 18, 223–226.
523 [https://doi.org/10.1130/0091-7613\(1990\)018<0223:RUACGI>2.3.CO;2](https://doi.org/10.1130/0091-7613(1990)018<0223:RUACGI>2.3.CO;2), 1990.

524 Bailey, E.H., and Ragnarsdottir, K.V.: Uranium and thorium solubilities in subduction zone fluids.
525 *Earth Planet. Sci. Lett.*, 124, 119–129. [https://doi.org/10.1016/0012-821X\(94\)00071-9](https://doi.org/10.1016/0012-821X(94)00071-9), 1994.

526 Beard, J.S., and Lofgren, G.E.: Dehydration melting and water-saturated melting of basaltic and
527 andesitic greenstones and amphibolites at 1, 3, and 6.9 kb. *J. Petrol.* 32, 365-401.
528 <https://doi.org/10.1093/petrology/32.2.365>, 1991.

529 BGMRH (Bureau of Geology and Mineral Resources of Henan Province): Geological map of the
530 Henan Province. Sheet I-49-(23) (Lushan) scale 1:200,000 (in Chinese), 1994.

531 Bonin, B.: Do coeval mafic and felsic magmas in post-collisional to within-plate regimes necessarily
532 imply two contrasting, mantle and crustal sources? A review. *Lithos*, 78, 1–24.
533 <https://doi.org/10.1016/j.lithos.2004.04.042>, 2004.

534 Carley, T.L., Miller, C.F., Wooden, J.L., Padilla, A.J., Schmitt, A.K., Economos, R.C., Bindeman, I.N.,
535 and Jordan, B.T.: Iceland is not a magmatic analog for the Hadean: evidence from the zircon record.
536 *Earth Planet. Sci. Lett.*, 405, 85-97. <https://doi.org/10.1016/j.epsl.2014.08.015>, 2014.

537 Castillo, P., Janney, P., and Solidum, R.: Petrology and geochemistry of Camiguin Island, southern
538 Philippines: insights to the source of adakites and other lavas in a complex arc setting. *Contrib.
539 Mineral. Petrol.*, 134, 33–51. <https://doi.org/10.1007/s004100050467>, 1999.

540 Chen, F., Hegner, E., and Todt, W.: Zircon ages, Nd isotopic and chemical compositions of
541 orthogneisses from the Black Forest, Germany - evidence for a Cambrian magmatic arc. *Int. J.
542 Earth Sci.*, 88, 791-802. <https://doi.org/10.1007/s005310050306>, 2000.

543 Chen, F., Li, X. H., Wang, X. L., Li, Q. L., and Siebel, W.: Zircon age and Nd-Hf isotopic composition
544 of the Yunnan Tethyan belt, southwestern China. *Int. J. Earth Sci.*, 96, 1179-1194.
545 <https://doi.org/10.1007/s00531-006-0146-y>, 2007.

546 Chen, L., Zheng, Y.F., Xu, Z., and Zhao, Z.F.: Generation of andesite through partial melting of basaltic
547 metasomatites in the mantle wedge: Insight from quantitative study of Andean andesites. *Geosci.
548 Front.*, 12, 101124. <https://doi.org/10.1016/j.gsf.2020.12.005>, 2021.

549 Cui, M.L., Zhang, B.L., Peng, P., Zhang, L.C., Shen, X.L., Guo, Z.H., and Huang, X.F.:
550 Zircon/baddeleyite U-Pb dating for the Paleoproterozoic intermediate-acid intrusive rocks in
551 Xiaoshan Mountains, west of Henan Province and their constraints on the age of the Xiong'er
552 Volcanic Province. *Acta Petrol. Sin. (in Chinese with English abstract)*, 26, 1541-1549, 2010.

553 Cui, M.L., Zhang, B.L., and Zhang, L.C.: U-Pb dating of baddeleyite and zircon from the Shizhaigou
554 diorite in the southern margin of North China Craton: Constraints on the timing and tectonic setting
555 of the Paleoproterozoic Xiong'er group. *Gondwana Res.*, 20, 184-193.
556 <https://doi.org/10.1016/j.gr.2011.01.010>, 2011.

557 Defant, M., and Drummond, M.: Derivation of some modern arc magmas by melting of young
558 subducted lithosphere. *Nature*, 347, 662-665. <https://doi.org/10.1038/347662a0>, 1990.

559 Deng, X. Q., Peng, T. P., and Zhao, T. P.: Geochronology and Geochemistry of the Late
560 Paleoproterozoic Aluminous A-Type Granite in the Xiaoqinling Area along the Southern Margin of
561 the North China Craton: Petrogenesis and Tectonic Implications. *Precambrian Res.*, 285: 127-146.
562 <https://doi.org/10.1016/j.precamres.2016.09.013>, 2016a

563 Deng, X.Q., Zhao, T.P., and Peng, T.P.: Age and geochemistry of the early Mesoproterozoic A-type
564 granites in the southern margin of the North China Craton: Constraints on their petrogenesis and
565 tectonic implications, *Precambrian Research*, 283, 68-88,
566 <https://doi.org/10.1016/j.precamres.2016.07.018>, 2016b.

567 Diwu, C.R., Liu, X., and Sun, Y.: The composition and evolution of the Taihua Complex in the
568 southern North China Craton. *Acta Petrol. Sin. (in Chinese with English abstract)*, 34, 999-1018,
569 2018.

570 Diwu, C.R., Sun, Y., Zhao, Y., and Lai, S.C.: Early Paleoproterozoic (2.45–2.20 Ga) magmatic activity
571 during the period of global magmatic shutdown: Implications for the crustal evolution of the
572 southern North China Craton. *Precambrian Res.*, 255, 627-640.
573 <https://doi.org/10.1016/j.precamres.2014.08.001>, 2014.

574 Fan, Y. H., Zhu, X. Y., Duan, Q. S., Ma, J. F., Jia, C. Y., Liu, S. Q., and Zhao, T. P.: Discovery of 1.79
575 Ga dacite porphyry in the Taiyueshan Mts: Constraints on the genesis of the southern rift system in
576 the North China Craton, *Acta Petrologica Sinica* (in Chinese with English abstract), 40(4), 1327–
577 1342, <https://doi.org/10.18654/1000-0569/2024.04.17>, 2024.

578 Gao, J.F., Zhou, M.F., Robinson, P.T., Wang, C.Y., Zhao, J.H., and Malpas, J.: Magma mixing recorded
579 by Sr isotopes of plagioclase from dacites of the Quaternary Tengchong volcanic field, SE Tibetan
580 Plateau. *J. Asian Earth Sci.*, 98, 1-17. <https://doi.org/10.1016/j.jseaes.2014.10.036>, 2015.

581 Geng, Y.S., Du, L.L., and Ren, L.D.: Growth and reworking of the early Precambrian continental crust
582 in the North China Craton: Constraints from zircon Hf isotopes. *Gondwana Res.*, 21, 517-529.
583 <https://doi.org/10.1016/j.gr.2011.07.006>, 2012.

584 Geng, Y. S., Yang, C. H., and Wan, Y. S.: Paleoproterozoic granitic magmatism in Lüliang area, North
585 China Craton: constraint from isotopic geochronology, *Acta Petrologica Sinica* (in Chinese with
586 English abstract), 22, 305–314, 2006.

587 Gorton, M.P., and Schandl, E.S.: From continents to island arcs: A geochemical index of tectonic
588 setting for arc-related and within-plate felsic to intermediate volcanic rocks. *Can. Mineral.*, 38,
589 1065–1073. <https://doi.org/10.2113/gscanmin.38.5.1065>, 2000.

590 Grimes, C.B., John, B.E., Kelemen, P.B., Mazdab, F., Wooden, J.L., Cheadle, M.J., Hanghøj, K., and
591 Schwartz, J.J.: Trace element chemistry of zircons from oceanic crust: a method for distinguishing
592 detrital zircon provenance. *Geology*, 35, 643-646. <https://doi.org/10.1130/G23603A.1>, 2007.

593 Hawkesworth, C.J., Norry, M.J., Roddick, J.C., Baker, P.E., Francis, P.W., and Thorpe, R.S.:
594 $^{143}\text{Nd}/^{144}\text{Nd}$, $^{87}\text{Sr}/^{86}\text{Sr}$, and incompatible element variations in calc-alkaline andesites and
595 plateau lavas from South America. *Earth Planet. Sci. Lett.*, 42, 45–57.
596 [https://doi.org/10.1016/0012-821X\(79\)90189-4](https://doi.org/10.1016/0012-821X(79)90189-4), 1979.

597 Hawkesworth, C.J., and Kemp, A.I.S.: Using hafnium and oxygen isotopes in zircons to unravel the
598 record of crustal evolution. *Chem. Geol.*, 226, 144-162.
599 <https://doi.org/10.1016/j.chemgeo.2005.09.018>, 2006.

600 He, J., Qi, Y., Fan, X., and Chen, F.: Petrogenesis of the Taishanmiao A-type granite in the eastern
601 Qinling orogenic belt: Implications for tectonic transition and mineralization in the Late Cretaceous.
602 *J. Geol.*, 129, 97-114. <https://doi.org/10.1086/713726>, 2021.

603 He, Y.H., Zhao, G.C., Sun, M., and Wilde, S.A.: Geochemistry, isotope systematics and petrogenesis of
604 the volcanic rocks in the Zhongtiao Mountain: An alternative interpretation for the evolution of the
605 southern margin of the North China Craton. *Lithos*, 102, 158-178.
606 <https://doi.org/10.1016/j.lithos.2007.09.004>, 2008.

607 He, Y.H., Zhao, G.C., Sun, M., and Xia, X.: SHRIMP and LA-ICP-MS zircon geochronology of the
608 Xiong'er volcanic rocks: Implications for the Paleo-Mesoproterozoic evolution of the southern
609 margin of the North China Craton. *Precambrian Res.*, 168, 213-222.
610 <https://doi.org/10.1016/j.precamres.2008.09.011>, 2009.

611 He, Y.H., Zhao, G.C., Sun, M., and Han, Y.G.: Petrogenesis and tectonic setting of volcanic rocks in the
612 Xiaoshan and Waifangshan areas along the southern margin of the North China Craton: Constraints
613 from bulk-rock geochemistry and Sr-Nd isotopic composition. *Lithos*, 114, 186-199.
614 <https://doi.org/10.1016/j.lithos.2009.08.008>, 2010.

615 Hickey, R.L., and Frey, F.A.: Geochemical characteristics of boninite series volcanics: implications for
616 their source. *Geochim. Cosmochim. Acta*, 46(11), 2099–2115.
617 [https://doi.org/10.1016/0016-7037\(82\)90188-0](https://doi.org/10.1016/0016-7037(82)90188-0), 1982.

618 Hou, G.T., Li, J.H., Yang, M.H., Yao, W.H., Wang, C.C., and Wang, Y.X.: Geochemical constraints on
619 the tectonic environment of the Late Paleoproterozoic mafic dyke swarms in the North China
620 Craton. *Gondwana Res.*, 13, 103-116. <https://doi.org/10.1016/j.gr.2007.06.005>, 2008.

621 Hoskin, P.W.O., Kinny, P.D., Wyborn, D., and Chappell, B.W.: Identifying accessory mineral saturation
622 during differentiation in granitoid magmas: an integrated approach. *J. Petrol.*, 41, 1365–1396.
623 <https://doi.org/10.1093/petrology/41.9.1365>, 2000.

624 Hu, G. H., Hu, J. L., Chen, W., and Zhao, T. P.: Geochemistry and tectonic setting of the 1.78 Ga mafic
625 dyke swarms in the Mt. Zhongtiao and Mt. Song areas, the southern margin of the North China
626 Craton, *Acta Petrologica Sinica* (in Chinese with English abstract), 26, 1563–1576, 2010.

627 Hu, G.Y., Zeng, L.S., Gao, L.E., Liu, Q.P., Chen, H., and Guo, Y.S.: Diverse magma sources for the
628 Himalayan leucogranites: Evidence from B-Sr-Nd isotopes. *Lithos*, 314-315, 88-99.
629 <https://doi.org/10.1016/j.lithos.2018.05.022>, 2018.

630 Huang, X.L., Xu, Y.G., and Liu, D.Y.: Geochronology, petrology and geochemistry of the granulite
631 xenoliths from Nushan, east China: implication for a heterogeneous lower crust beneath the
632 Sino-Korean Craton. *Geochim. Cosmochim. Acta*, 68, 127-149.
633 [https://doi.org/10.1016/S0016-7037\(03\)00416-2](https://doi.org/10.1016/S0016-7037(03)00416-2), 2004.

634 Jackson, M.D., Cheadle, M.J., and Atherton, M.P.: Quantitative modeling of granitic melt generation
635 and segregation in the continental crust. *J. Geophys. Res. Solid Earth*, 108, 2332.
636 <https://doi.org/10.1029/2001JB001050>, 2003.

637 Jia, C.Z., Petro-geochemistry of volcanic rocks in the Xiong'er Group: implications for tectonic setting.
638 *Henan Geol.* 2:39–43 (in Chinese with English abstract), 1985.

639 Jochum, K.P., Seufert, H.M., Spettel, B., and Palme, H.: The solar-system abundances of Nb, Ta, and Y,
640 and the relative abundances of refractory lithophile elements in differentiated planetary bodies.
641 *Geochim. Cosmochim. Acta*, 50, 1173-1183. [https://doi.org/10.1016/0016-7037\(86\)90400-X](https://doi.org/10.1016/0016-7037(86)90400-X), 1986.

642 Kelemen, P.B.: Genesis of high Mg[#] andesites and the continental crust. *Contrib. Mineral. Petrol.*, 120,
643 1-19. <https://doi.org/10.1007/BF00311004>, 1995.

644 Kröner, A., Compston, W., Zhang, G.-W., Guo, A.-L., and Todt, W.: Age and tectonic setting of Late
645 Archean greenstone-gneiss terrain in Henan Province, China, as revealed by single-grain zircon
646 dating. *Geology*, 16, 211–215,
647 [https://doi.org/10.1130/0091-7613\(1988\)016<211:AATSOL>2.3.CO;2](https://doi.org/10.1130/0091-7613(1988)016<211:AATSOL>2.3.CO;2), 1988.

648 Le Bas, M.J., Le Maitre, R.W., Streckeisen, A., and Zanettin, B.: A Chemical Classification of
649 Volcanic-Rocks Based on the Total Alkali Silica Diagram. *J. Petrol.*, 27, 745-750.
650 <https://doi.org/10.1093/petrology/27.3.745>, 1986.

651 Li, X. P., Yang, Z. Y., Zhao, G. C., Grapes, R., and Guo, J. H.: Geochronology of khondalite-series
652 rocks of the Jining Complex: Confirmation of depositional age and tectonometamorphic evolution
653 of the North China craton, *Int. Geol. Rev.*, 53, 1194–1211, doi:10.1080/00206810903548984, 2011.

654 Liu, A.L., Hai, L.F., Liu, J.K., Zhang X.J., Li H.F., Zhao F.S., Zhao G.L., and Bai J.H.: Geochronology,
655 Geochemistry, and Sr-Nd-Hf Isotopes of the Diorite Porphyrites from the Weining Beishan Area,
656 Ningxia Hui Autonomous Region: Constraints on Their Source and Tectonic Implications. *J. Earth*
657 *Sci.* 35, 462–475. <https://doi.org/10.1007/s12583-021-1491-2>, 2024.

658 Liu, D.Y., Nutman, A.P., Compston, W., Wu, J.S., and Shen, Q.H.: Remnants of \geq 3800 Ma crust in the
659 Chinese part of the Sino-Korean Craton. *Geology*, 20, 339-342.
660 [https://doi.org/10.1130/0091-7613\(1992\)020<0339:ROMCIT>2.3.CO;2](https://doi.org/10.1130/0091-7613(1992)020<0339:ROMCIT>2.3.CO;2), 1992.

661 Liu, Y.S., Hu, Z.C., Zong, K.Q., Gao, C.G., Gao, S., Xu, J.A., and Chen, H.H.: Reappraisal and
662 refinement of zircon U-Pb isotope and trace element analyses by LA-ICP-MS. *Chin. Sci. Bull.* (in
663 Chinese with English abstract), 1535-1546, 2010.

664 Lu, S.N., Zhao, G.C., Wang, H.C., and Hao, G.J.: Precambrian metamorphic basement and sedimentary
665 cover of the North China Craton: A review. *Precambrian Res.*, 160, 77–93, 2008.

666 Luo, Y., Sun, M., Zhao, G. C, Li, S.Z., Xu, P., Ye, K., and Xia, X.P.: LA-ICP-MS U–Pb zircon ages of
667 the Liaohe Group in the Eastern Block of the North China Craton: constraints on the evolution of
668 the Jiao-Liao-Ji Belt, *Precambrian Research*, 134(3-4), 349-371,
669 <https://doi.org/10.1016/j.precamres.2004.07.002>, 2004.

670 Ma, J.F., Qu, C.H., Zhou, Y.Y., and Zhao, T.P.: The genesis of *ca.* 1.78 Ga granitoids in the Xiong'er
671 large igneous province: Implications for continental crust generation. *Geol. Soc. Am. Bull.*, 135,
672 3213-3227. <https://doi.org/10.1130/B36694.1>, 2023a.

673 Ma, J.F., Wang, X.L., Yang, A.Y., and Zhao, T.P.: Tracking crystal-melt segregation and accumulation
674 in the intermediate magma reservoir. *Geophys. Res. Lett.*, 50, e2022GL102540.
675 <https://doi.org/10.1029/2022GL102540>, 2023b.

676 Maniar, P.D., and Piccoli, P.M.: Tectonic discrimination of granitoids. *Geol. Soc. Am. Bull.*, 101,
677 635-643. [https://doi.org/10.1130/0016-7606\(1989\)101<0635:TDOG>2.3.CO;2](https://doi.org/10.1130/0016-7606(1989)101<0635:TDOG>2.3.CO;2), 1989.

678 Pan, Z.J., Zhang, Q., Chen, G., Jiao, S.T., Du, X.L., Miao, X.Q., Wang, J.R., and An, Y.: Relation
679 between Mesozoic magmatism and plate subduction in eastern China: Comparison among
680 Zhejiang-Fujian, Japan arc and Andes arc. *Acta Petrol. Sin.* (in Chinese with English abstract), 33,
681 1507–1523, 2017.

682 Peacock, S.M., Rushmer, T., and Thompson, A.B.: Partial melting of subducting oceanic crust. *Earth*
683 *Planet. Sci. Lett.*, 121, 227-244. [https://doi.org/10.1016/0012-821X\(94\)90042-6](https://doi.org/10.1016/0012-821X(94)90042-6), 1994.

684 Pearce, J.A.: Role of the sub-continental lithosphere in magma genesis at active continental margins.
685 In: Hawkesworth, C.J., Norry, M.J. (Eds.): *Continental Basalts and Mantle Xenoliths*. Shiva
686 Publishing Ltd., Nantwich, 230–249. ISBN: 978-0906812341, 1983.

687 Pearce, J.A., and Peate, D.W.: Tectonic implications of the composition of volcanic arc magmas. *Annu.*
688 *Rev. Earth Planet. Sci.*, 23, 251–285. <https://doi.org/10.1146/annurev.ea.23.050195.001343>, 1995.

689 Peccerillo, A., and Taylor, S.R.: Geochemistry of Eocene calc-alkaline volcanic rocks from the
690 Kastamonu area, northern Turkey. *Contrib. Mineral. Petrol.*, 58, 130–143.
691 <https://doi.org/10.1007/BF00384745>, 1976.

692 Peng, P., Zhai, M.G., Zhang, H.F., Zhao, T.P., and Ni, Z.Y.: Geochemistry and geological significance
693 of the 1.8 Ga mafic dyke swarms in the North China Craton: an example from the juncture of
694 Shanxi, Hebei and Inner Mongolia. *Acta Petrol. Sin.* (in Chinese with English abstract), 20,
695 439-456, 2004.

696 Peng, P., Zhai, M.G., Guo, J.H., Kusky, T., and Zhao, T.P.: Nature of mantle source contributions and
697 crystal differentiation in the petrogenesis of the 1.78 Ga mafic dykes in the central North China
698 craton. *Gondwana Res.*, 12, 29-46. <https://doi.org/10.1016/j.gr.2006.10.022>, 2007.

699 Peng, P., Zhai, M.G., Ernst, R.E., Guo, J.H., Liu, F., and Hu, B.: A 1.78 Ga large igneous province in
700 the North China craton: The Xiong'er Volcanic Province and the North China dyke swarm. *Lithos*,
701 101, 260-280. <https://doi.org/10.1016/j.lithos.2007.07.006>, 2008.

702 Petford, N., and Atherton, M.: Na-rich partial melts from newly underplated basaltic crust: the
703 Cordillera Blanca Batholith, Peru. *J. Petrol.*, 37, 1491-1521.
704 <https://doi.org/10.1093/petrology/37.6.1491>, 1996.

705 Rapp, R.P., and Watson, E.B.: Dehydration melting of metabasalt at 8–32 kbar: Implications for
706 continental growth and crust-mantle recycling. *J. Petrol.*, 36, 891-931.
707 <https://doi.org/10.1093/petrology/36.4.891>, 1995.

708 Reubi, O., and Blundy, J.: A dearth of intermediate melts at subduction zone volcanoes and the
709 petrogenesis of arc andesites. *Nature*, 461, 1269-1273. <https://doi.org/10.1038/nature08510>, 2009.

710 Roberts, M.P., and Clemens, J.D.: Origin of high-potassium, calc-alkaline, I-type granitoids. *Geology*,
711 21, 825–828. [https://doi.org/10.1130/0091-7613\(1993\)021<0825:OOHPTA>2.3.CO;2](https://doi.org/10.1130/0091-7613(1993)021<0825:OOHPTA>2.3.CO;2), 1993.

712 Schulz, B., Klemd, R., and Brätz, H.: Host rock compositional controls on zircon trace element
713 signatures in metabasites from the Austroalpine basement. *Geochim. Cosmochim. Acta*, 70, 697–
714 710. <https://doi.org/10.1016/j.gca.2005.10.001>, 2006.

715 Shannon, R.D.: Revised effective ionic-radii and systematic studies of interatomic distances in halides
716 and chalcogenides. *Acta Crystallogr. A*, 32, 751-767. <https://doi.org/10.1107/S0567739476001551>,
717 1976.

718 Shen, F.N.: The discovery of unconformity within the Taihua Group and definition of its stratigraphic
719 sequence in the Lushan area, Henan. *Reg. Geol. China* (in Chinese with English abstract), 2,
720 135-140. doi: 10.12097/gbc.ZQYD402.005, 1994.

721 Siebel, W., Reitter, E., Wenzel, T., and Blaha U.: Sr isotope systematics of K-feldspars in plutonic rocks
722 revealed by the Rb–Sr microdrilling technique. *Chem. Geol.*, 222, 183–199.
723 <https://doi.org/10.1016/j.chemgeo.2005.06.012>, 2005.

724 Stern, C., and Kilian, R.: Role of the subducted slab, mantle wedge and continental crust in the
725 generation of adakites from the Andean Austral Volcanic Zone. *Contrib. Mineral. Petrol.*, 123,
726 263-281. <https://doi.org/10.1007/s004100050155>, 1996.

727 Streck, M.J., Leeman, W.P., and Chesley, J.: High-magnesian andesite from Mount Shasta: A product of
728 magma mixing and contamination, not a primitive mantle melt. *Geology*, 35, 351-354.
729 <https://doi.org/10.1130/G23286A.1>, 2007.

730 Sun, Q.Y., Zhou, Y.Y., Wang, W., Li, C.D., and Zhao, T.P.: Formation and evolution of the
731 Paleoproterozoic meta-mafic and associated supracrustal rocks from the Lushan Taihua Complex,
732 southern North China Craton: Insights from zircon U-Pb geochronology and whole-rock
733 geochemistry. *Precambrian Res.*, 303, 428-444. <https://doi.org/10.1016/j.precamres.2017.05.018>,
734 2017.

735 Sun, S.S., and McDonough, W.F.: Chemical and isotopic systematics of oceanic basalts: implications
736 for mantle composition and processes. *Geol. Soc. London, Spec. Publ.*, 42, 313-345.
737 <https://doi.org/10.1144/GSL.SP.1989.042.01.19>, 1989.

738 Vermesch, P.: IsoplotR: A free and open toolbox for geochronology. *Geoscience Frontiers*, 9,
739 1479-1493. <https://doi.org/10.1016/j.gsf.2018.04.001>, 2018.

740 Wan, Y.S., Wlide, S., Liu, D.Y., Yang, C.X., Song, B., and Yin, X.Y.: Further evidence for ~1.85 Ga
741 metamorphism in the Central Zone of the North China Craton: SHRIMP U-Pb dating of zircon
742 from metamorphic rocks in the Lushan area, Henan Province. *Gondwana Res.*, 9, 189-197,
743 <https://doi.org/10.1016/j.gr.2005.06.010>, 2006

744 Wang, C.M., Lu, Y.J., He, X.Y., Wang, Q.H., and Zhang, J.: The Paleoproterozoic diorite dykes in the
745 southern margin of the North China Craton: Insight into rift-related magmatism. *Precambrian Res.*,
746 277, 26-46. <https://doi.org/10.1016/j.precamres.2016.02.009>, 2016.

747 Wang, J.L., Zhang, H.F., Zhang, J., Santosh, M., and Bao, Z. A.: Highly heterogeneous Pb isotope
748 composition in the Archean continental lower crust: Insights from the high-grade metamorphic suite
749 of the Taihua Group, Southern North China Craton. *Precambrian Res.*, 350, 105927.
750 <https://doi.org/10.1016/j.precamres.2020.105927>, 2020.

751 Wang, M.X., Wang Z.Y., Zhao J.X., Qi Z.Q., He J., and Chen F.K.: Petrogenesis and Geologic
752 Implication of the Late Paleoproterozoic A-type Xiaohe Pluton along the Southern Margin of the
753 North China Craton. *Geol. J. China Univ. (in Chinese with English abstract)*, 29(6): 809-830, 2023a.

754 Wang, X., Huang X., and Yang F.: Revisiting the Lushan-Taihua Complex: New perspectives on the
755 Late Mesoarchean-Early Neoarchean crustal evolution of the southern North China Craton:
756 Precambrian Res., 325, 132–149. <https://doi.org/10.1016/j.precamres.2019.02.020>, 2019.

757 Wang, X.W., Zhu, M. Luo, X. Ren, and X. Cui.: Approximately 1.78 Ga mafic dykes in the Lüliang
758 Complex, North China Craton: Zircon ages and Lu-Hf isotopes, geochemistry, and implications,
759 *Geochem. Geophys. Geosyst.*, 15, 3123–3144. doi:10.1002/2014GC005378, 2014.

760 Wang, X.L., Jiang, S.Y., and Dai, B.Z.: Melting of enriched Archean subcontinental lithospheric
761 mantle: Evidence from the *ca.* 1760 Ma volcanic rocks of the Xiong'er Group, southern margin of
762 the North China Craton. *Precambrian Res.*, 182, 204–216.
763 <https://doi.org/10.1016/j.precamres.2010.08.007>, 2010.

764 Wang, Y.J., Fan, W.M., Zhang, Y., Guo, F., Zhang, H., and Peng, T.: Geochemical, $^{40}\text{Ar}/^{39}\text{Ar}$
765 geochronological and Sr-Nd isotopic constraints on the origin of Paleoproterozoic mafic dikes from
766 the southern Taihang Mountains and implications for the *ca.* 1800 Ma event of the North China
767 Craton. *Precambrian Res.*, 135, 55-77. <https://doi.org/10.1016/j.precamres.2004.07.005>, 2004.

768 Wang, Y., Zhao, G., Cawood, P. A., Fan, W., Peng, T., and Sun, L.: Geochemistry of Paleoproterozoic
769 (\sim 1770 Ma) mafic dikes from the Trans-North China Orogen and tectonic implications, *J. Asian*
770 *Earth Sci.* 33(1–2), 61–77, <https://doi.org/10.1016/j.jseaes.2007.10.018>, 2008.

771 Wang, Z.Y., Zhao, J.X., Qi, Z.Q., Huo, D.Y., Siebel, W., He, J., Li, S.Q., and Chen, F.C.: Two stages of
772 late Paleoproterozoic A-type granites at the southern North China Craton: Geochemical constraints
773 and implications for supercontinent breakup, *Precambrian Research*, 411, 107500,
774 <https://doi.org/10.1016/j.precamres.2024.107500>, 2024.

775 Wang, Z.Y., Cheng, H., Zhao, J.X., Ye R.S., Li W.Y., He J.F., and Chen F.K.: Sr-Nd-Pb isotopic
776 composition of the Chinese national standard igneous rock powders measured by thermal ionization
777 mass spectrometry. *Geol. J. China Univ. (in Chinese with English abstract)*, 29, 679-692, 2023b.

778 Wolf, M.B., and Wyllie, P.J.: Garnet growth during amphibolite anatexis: Implications of a
779 garnetiferous restite. *J. Geol.*, 101, 357-373. <https://doi.org/10.1086/648229>, 1993.

780 Wolf, M., Romer, R.L., and Glodny, J.: Isotope disequilibrium during partial melting of
781 metasedimentary rocks. *Geochim. Cosmochim. Acta* 257, 163-183.
782 <https://doi.org/10.1016/j.gca.2019.05.008>, 2019.

783 Xu, J.H., Jiang, Y.P., Hu, S.L., Zhang Z.W., Wu C.Q., Zheng C.F., Li X.Y., Jin Z.R., Zhang S.S., and
784 Zhou Y.T.: Petrogenesis and Tectonic Implications of the Paleoproterozoic A-Type Granites in the
785 Xiong'ershan Area along the Southern Margin of the North China Craton. *J. Earth Sci.*, 35, 416–
786 429. <https://doi.org/10.1007/s12583-021-1424-0>, 2024.

787 Xu, Y.H., Zhao, T.P., Zhang, Y.X., and Chen, W.: Geochemical characteristics and geological
788 significance of the detrital rocks from the Dagushi Formation of the Paleoproterozoic Xiong'er
789 Group in the southern North China Craton, *Geological Review*, 54(3), 316–326,
790 <https://doi.org/10.3321/j.issn:0371-5736.2008.03.004>, 2008.

791 Xue, L.W., Yuan, Z.L., Zhang, M.S., and Qiang, L.Z.: The Sm-Nd isotope ages of Tai-hua Group in the
792 Lushan area and their implications. *Geochimica* (in Chinese with English abstract), 24, 92-97, 1995.

793 Yang, J.H., Cawood, P.A., Du, Y.S., Huang, H., Huang, H.W., and Tao, P.: Large Igneous Province and
794 magmatic arc sourced Permian–Triassic volcanogenic sediments in China. *Sedimentary Geol.*
795 261-262, 120-131. <https://doi.org/10.1016/j.sedgeo.2012.03.018>, 2012.

796 Yang, Z.M., Lu, Y.J., Hou, Z.Q., and Chang, Z.S.: High-Mg diorite from Qulong in southern Tibet:
797 implications for the genesis of adakite-like intrusions and associated porphyry Cu deposits in
798 collisional orogens. *J. Petrol.*, 56, 227–254. <https://doi.org/10.1093/petrology/egu076>, 2015.

799 Zeng, L.S., Asimow, P.D., and Saleeby, J.B.: Coupling of anatetic reactions and dissolution of
800 accessory phases and the Sr and Nd isotope systematics of anatetic melts from a metasedimentary
801 source. *Geochim. Cosmochim. Acta*, 69, 3671-3682. <https://doi.org/10.1016/j.gca.2005.02.035>,
802 2005.

803 Zhai, M.G.: Tectonic evolution and metallogenesis of North China Craton. *Mineral Deposits* (in
804 Chinese with English abstract), 29, 24-36, 2010.

805 Zhai M G.: Cratonization and the Ancient North China Continent: A summary and review. *Sci China*
806 *Earth Sci* (in Chinese with English abstract), 54: 1110–1120, doi: 10.1007/s11430-011-4250-x,
807 2011.

808 Zhao, G.C., Cawood, P.A., Wilde, S.A., Min, S., and Lu, L.Z.: Metamorphism of basement rocks in the
809 Central Zone of the North China Craton: implications for Paleoproterozoic tectonic evolution.
810 *Precambrian Res.*, 103, 55-88. [https://doi.org/10.1016/S0301-9268\(00\)00076-0](https://doi.org/10.1016/S0301-9268(00)00076-0), 2000a.

811 Zhao, G.C., He, Y.H., and Sun, M.: Xiong'er volcanic belt at the North China Craton: The Xiong'er
812 volcanic belt at the southern margin of the North China Craton: Petrographic and geochemical
813 evidence for its outboard position in the Paleo-Mesoproterozoic Columbia Supercontinent.
814 *Gondwana Res.*, 16, 170–181. <https://doi.org/10.1016/j.gr.2009.02.004>, 2009.

815 Zhao, G.C., Wilde, S.A., Cawood, P.A., and Lu, L.Z.: Petrology and P-T path of the Fuping mafic
816 granulites: implications for tectonic evolution of the central zone of the North China Craton. *J.*
817 *Metamorphic Geol.*, 18, 375-391. <https://doi.org/10.1046/j.1525-1314.2000.00264.x>, 2000b.

818 Zhao, G.C., Wilde, S.A., Cawood, P.A., and Sun, M.: Archean blocks and their boundaries in the North
819 China Craton: lithological, geochemical, structural and P-T path constraints and tectonic evolution.
820 *Precambrian Res.* 107, 45-73. [https://doi.org/10.1016/S0301-9268\(00\)00154-6](https://doi.org/10.1016/S0301-9268(00)00154-6), 2001.

821 Zhao, G.C., Wilde, S. A., Sun, M., Li, S., Li, X., and Zhang, J.: SHRIMP U–Pb zircon ages of granitoid
822 rocks in the Lüliang Complex: Implications for the accretion and evolution of the Trans-North
823 China Orogen, *Precambrian Research*, 160(3–4), 213–226,
824 <https://doi.org/10.1016/j.precamres.2007.07.004>, 2008.

825 Zhao, G.C., Sun, M., Wilde, S.A., and Li Sanzhong.: Late Archean to Paleoproterozoic evolution of the
826 North China Craton: key issues revisited. *Precambrian Res.*, 136, 177-202
827 <https://doi.org/10.1016/j.precamres.2004.10.002>, 2005.

828 Zhao, G.C., and Zhai, M.G.: Lithotectonic elements of Precambrian basement in the North China
829 Craton: Review and tectonic implications. *Gondwana Res.*, 23, 1207-1240.
830 <https://doi.org/10.1016/j.gr.2012.08.016>, 2013.

831 Zhao, J., Zhang, C., Guo, X., and Liu, X.: The late-Paleoproterozoic I- and A-type granites in Lüliang
832 Complex, North China Craton: New evidence on post-collisional extension of Trans-North China
833 Orogen, *Precambrian Research*, 318, 70–88, <https://doi.org/10.1016/j.precamres.2018.09.007>, 2018.

834 Zhao, T.P.: The characteristic and genesis of Proterozoic potassic volcanic rock in southern margin of
835 the North plate. Doctoral dissertation, Institute of Geology and Geophysics, Chinese Academy of
836 Sciences, Beijing, 102p, 2000.

837 Zhao, T.P., Xu, Y.H., and Zhai, M.G.: Petrogenesis and tectonic setting of the Paleoproterozoic
838 Xiong'er Group in the southern part of the North China Craton: A review. *Geol. J. China Univ.* (in
839 Chinese with English abstract), 13, 191–206, 2007.

840 Zhao, T.P., Zhou, M.F., Zhai, M.G., and Xia, B.: Paleoproterozoic rift-related volcanism of the Xiong'er
841 Group, North China Craton: Implications for the breakup of Columbia. *Int. Geol. Rev.*, 44, 336-351.
842 <https://doi.org/10.2747/0020-6814.44.4.336>, 2002

843 Zhao, T.P., Zhai, M.G., Xia, B., Li, H.M., and Zhang, Y.X.: Zircon U-Pb SHRIMP dating for the
844 volcanic rocks of the Xiong'er Group: Constraints on the initial formation age of the cover of the
845 North China Craton. *Chin. Sci. Bull.* (in Chinese with English abstract), 49, 2495–2502, 2004.

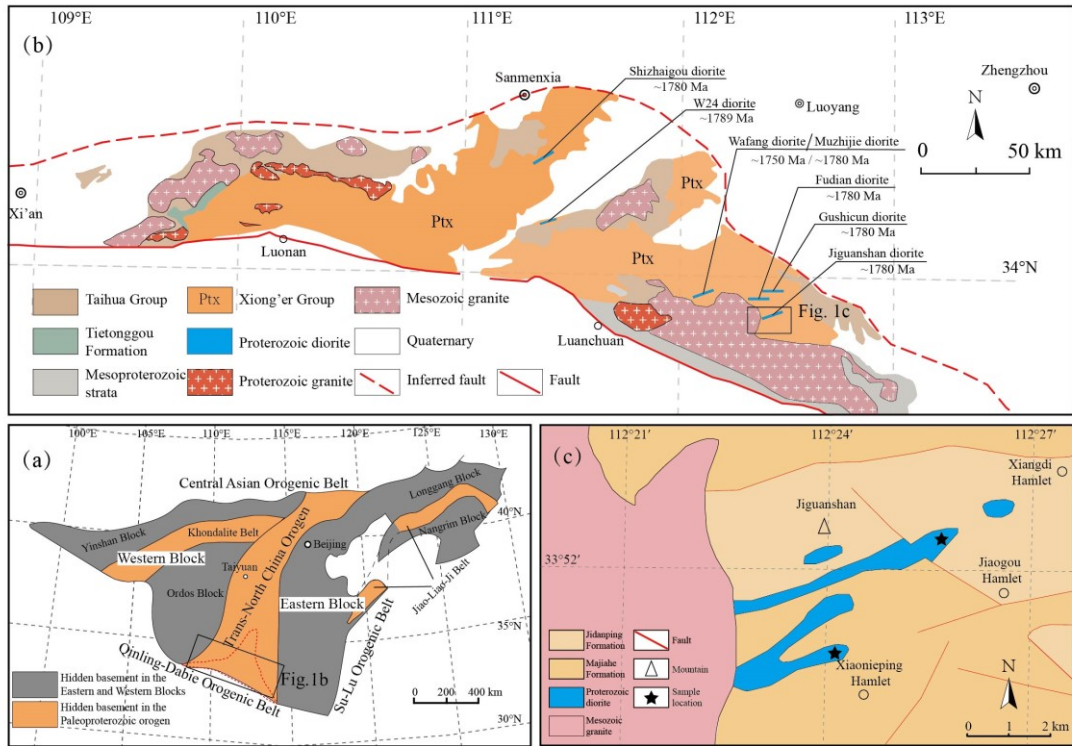
846 Zhang, G.W., Bai, Y.B., Sun, Y., Guo, A.L., Zhou, D.W., and Li, T.H.: Composition and evolution of
847 the Archaean crust in central Henan, China. *Precambrian Res.*, 27, 7-35.
848 [https://doi.org/10.1016/0301-9268\(85\)90004-X](https://doi.org/10.1016/0301-9268(85)90004-X), 1985.

849 Zou, X.Y., Qin, K.Z., Han, X.L., Li, G.M., Evans, N.J., Li, Z.Z., and Yang, W.: Insight into zircon REE
850 oxy-barometers: A lattice strain model perspective. *Earth Planet. Sci. Lett.*, 506, 87-96.
851 <https://doi.org/10.1016/j.epsl.2018.10.031>, 2019.

852

853

854 **Figure captions**

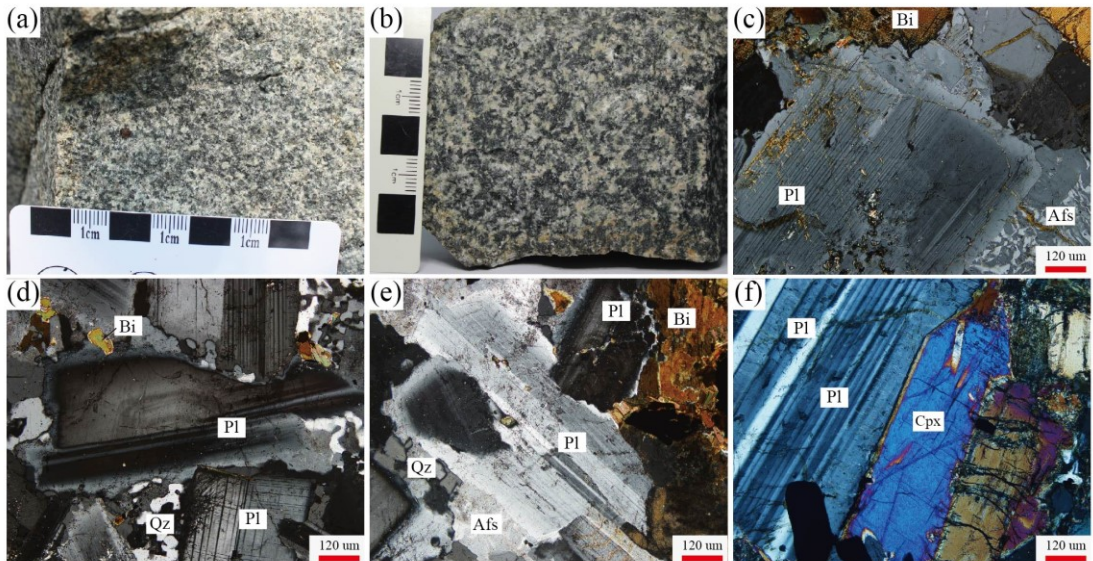


855

856 **Figure 1** (a) Tectonic sketch of the North China Craton (after Zhao et al., 2001); (b) Geological
 857 map of the southern margin of the North China Craton (after Diwu et al., 2014; diorites from
 858 Cui et al., 2011; Ma et al 2023a, b; Wang et al., 2016; Zhao et al., 2004); (c) Geological map of
 859 the Jiguanshan diorite (after BGMRH, 1994)

860

861

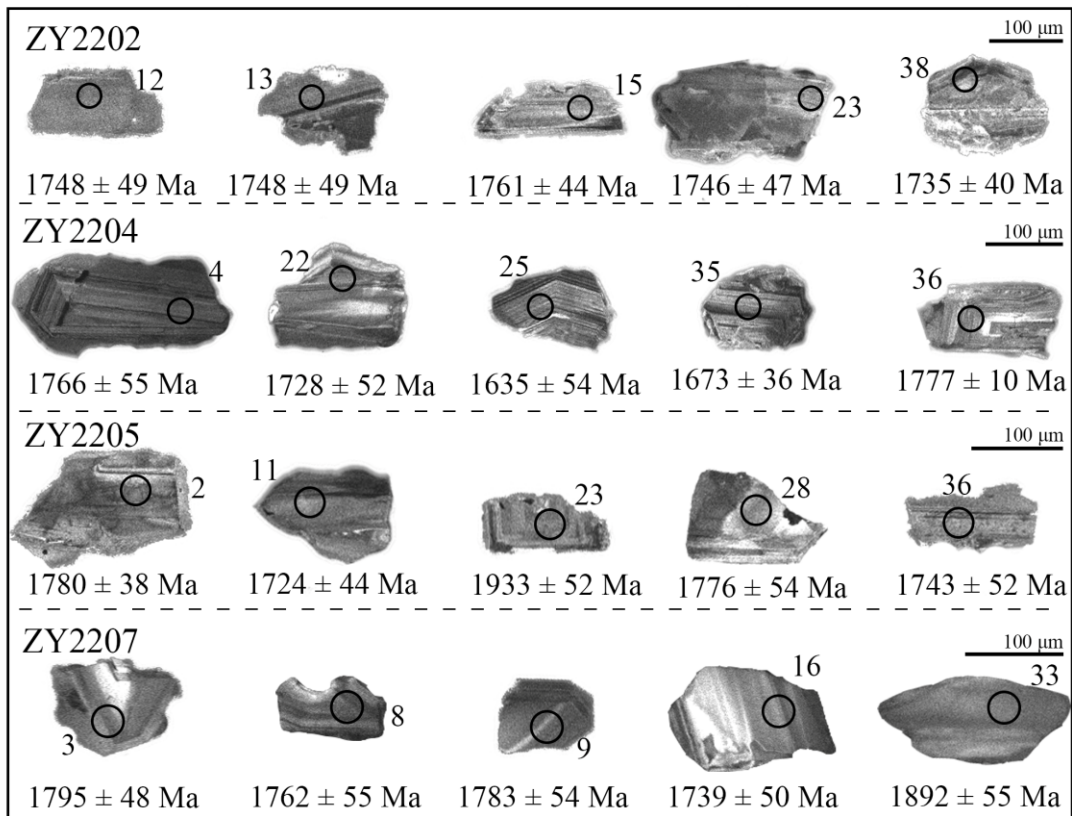


862

863 **Figure 2** (a-b) Field photographs and representative hand specimens of the Jiguanshan diorite; (c-f)
 864 Microphotographs under plane-polarized light of the Jiguanshan diorite. Mineral
 865 abbreviations: Afs, alkali feldspar; Bi, biotite; Cpx, Clinopyroxene; Pl, plagioclase; Qz,
 866 quartz

867

868

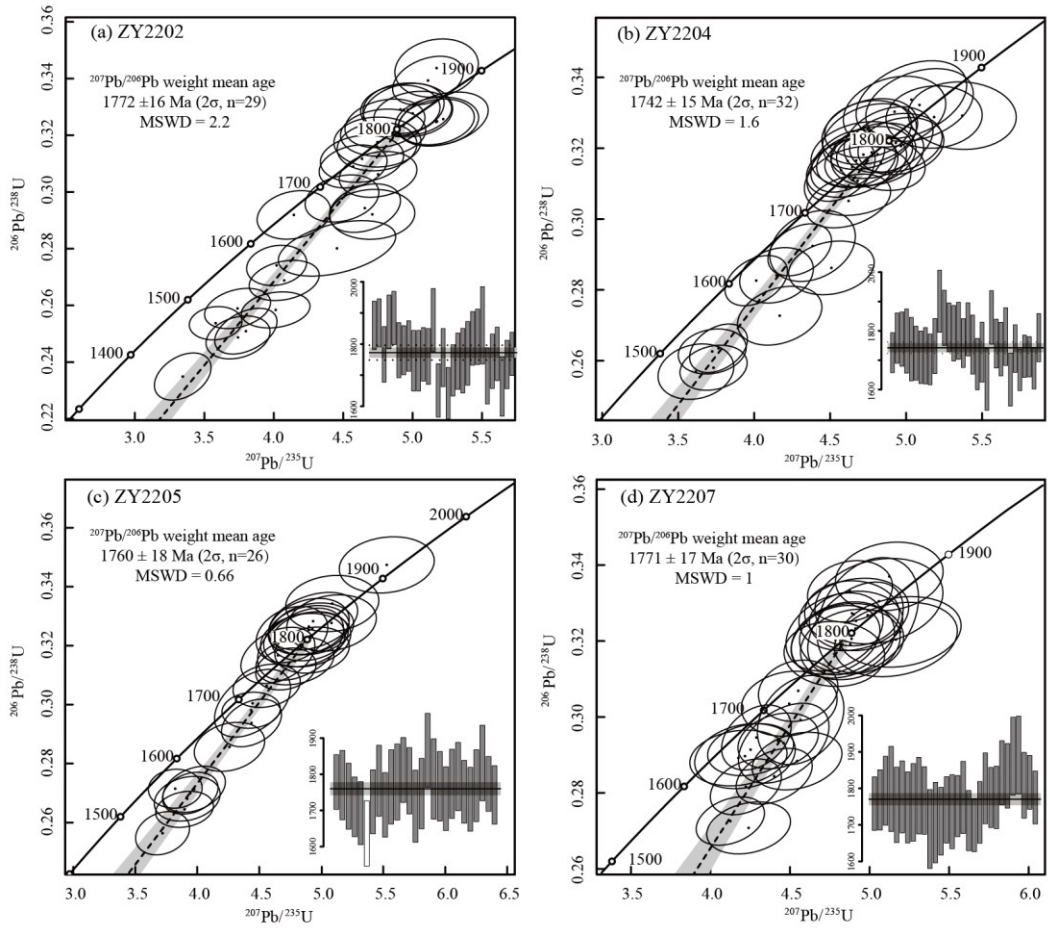


869

870 **Figure 3** Cathodoluminescence (CL) images of representative zircon grains from the Jiguanshan

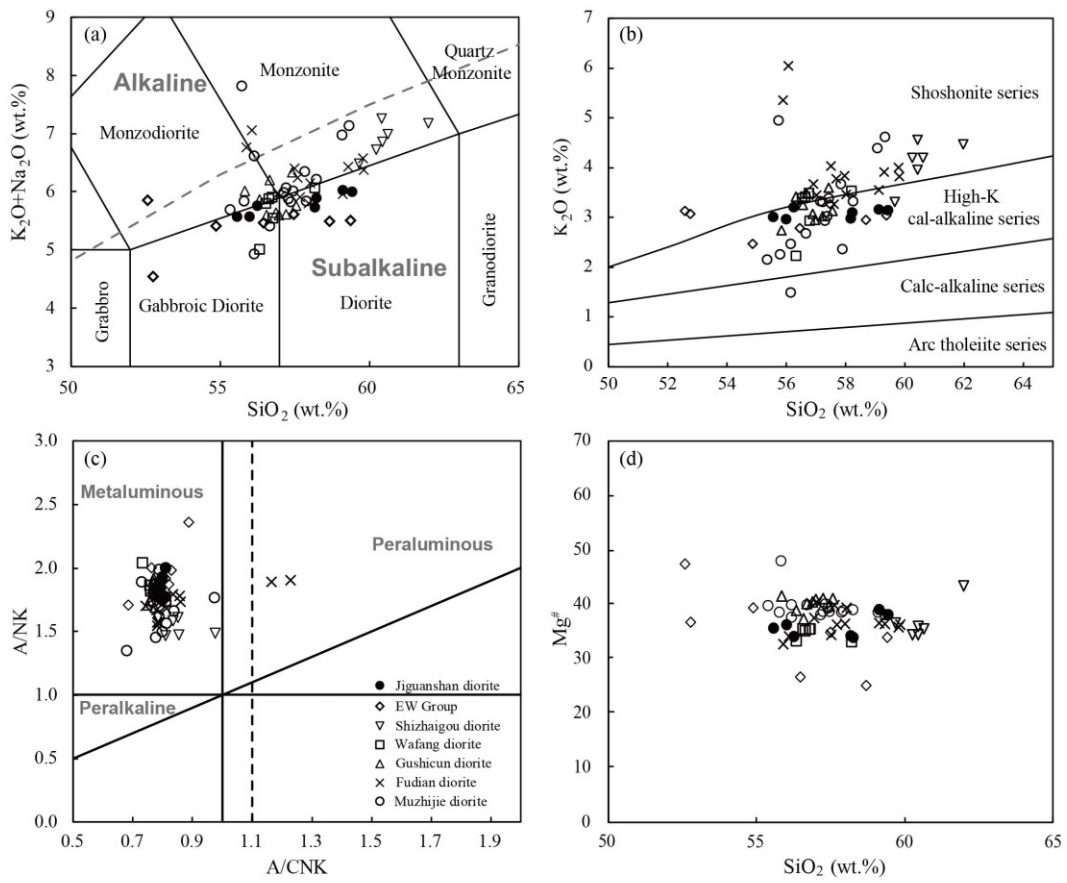
871 diorite

872



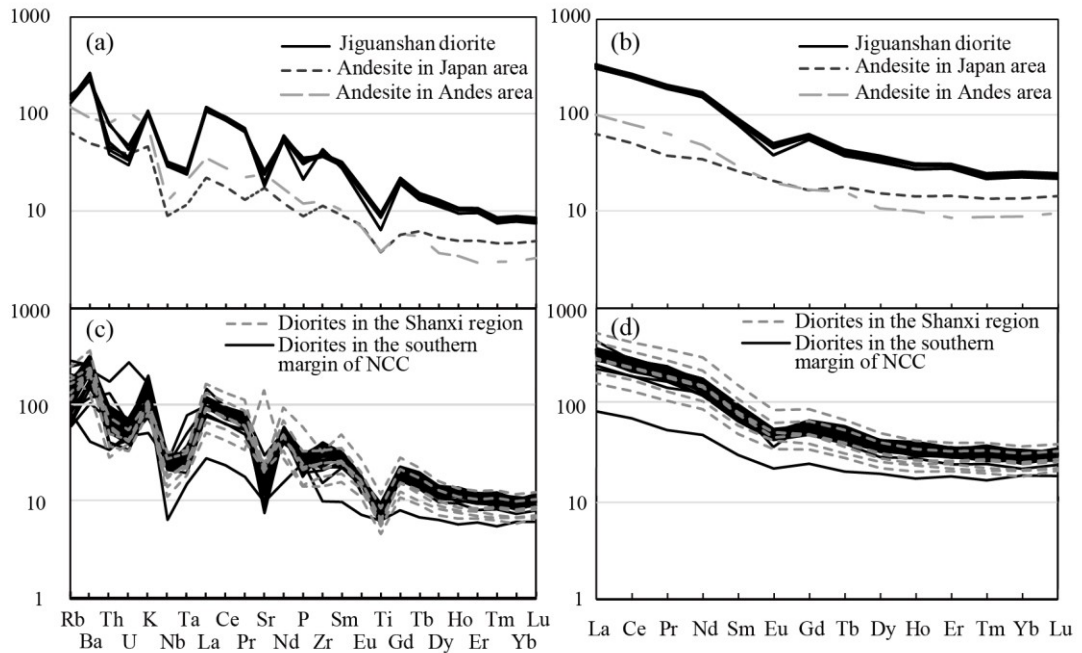
873

874 **Figure 4 (a-d)** Zircon U-Pb Concordia diagrams for the Jiguanshan diorite



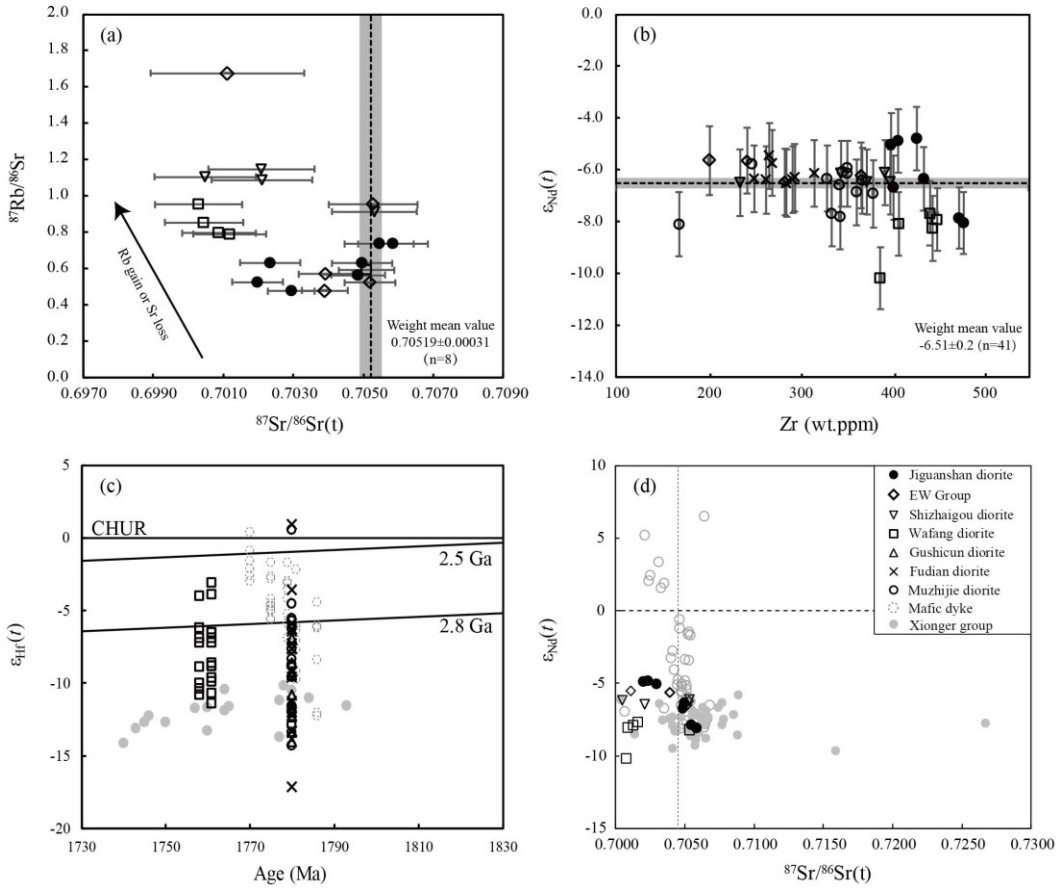
875

876 **Figure 5** Plots of major elements for the diorites: (a) TAS diagram (after [Le Bas et al., 1986](#)); (b)
 877 K_2O content versus SiO_2 content (after [Peccerillo and Taylor, 1976](#)); (c) A/NK versus A/CNK
 878 values (after [Maniar and Piccoli, 1989](#)) (d) $Mg^{\#}$ value versus SiO_2 content (wt. %)



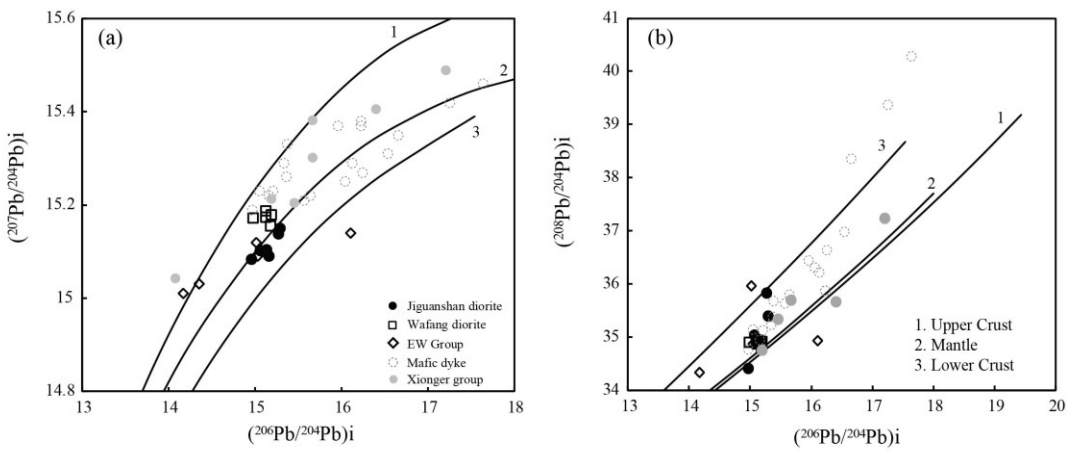
879

880 **Figure 6** Primitive-mantle normalized trace element spider diagrams and chondrite-normalized
 881 REE patterns for the diorites. Normalization values from [Sun and McDonough \(1989\)](#);
 882 Diorites in Shanxi region from [Peng et al. \(2007\)](#), diorites in the southern margin of the NCC
 883 from [Cui et al. \(2011\)](#), [Ma et al. \(2023a, b\)](#), [Wang et al. \(2016\)](#), and [Zhao et al. \(2004\)](#).
 884 Average trace element compositions of intermediate rocks in the Japan and Andes arc are
 885 from [Pan et al. \(2017\)](#)



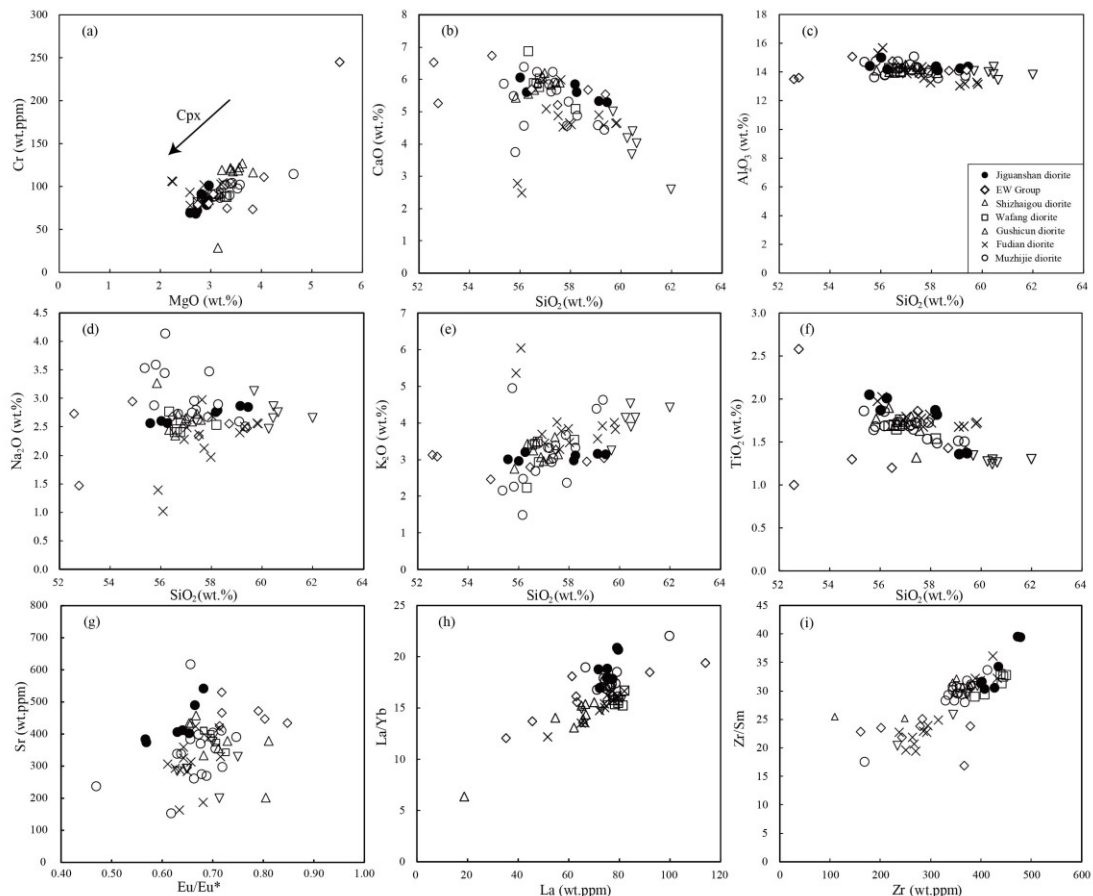
886

887 **Figure 7** (a) $^{87}\text{Rb}/^{86}\text{Sr}$ versus $^{87}\text{Sr}/^{86}\text{Sr(t)}$ ratio; (b) $\varepsilon_{\text{Nd}}(t)$ value versus Zr content (ppm); (c) $\varepsilon_{\text{Nd}}(t)$ value versus age (Ma); (d) $\varepsilon_{\text{Nd}}(t)$ value versus $^{87}\text{Sr}/^{86}\text{Sr(t)}$ ratio. Data source for Xiong'er
 888 Group (Hf isotope composition from [Wang et al., 2010](#); initial Sr isotope composition and
 889 initial ε_{Nd} value from [He et al., 2008, 2010](#); [Peng et al., 2008](#); [Wang et al., 2010](#); [Zhao et al.,](#)
 890 [2002](#)); mafic dyke swarms (initial Sr isotope composition and initial ε_{Nd} value from [Hu et al.,](#)
 891 [2010](#); [Peng et al., 2007](#); [Wang et al., 2004](#))



893

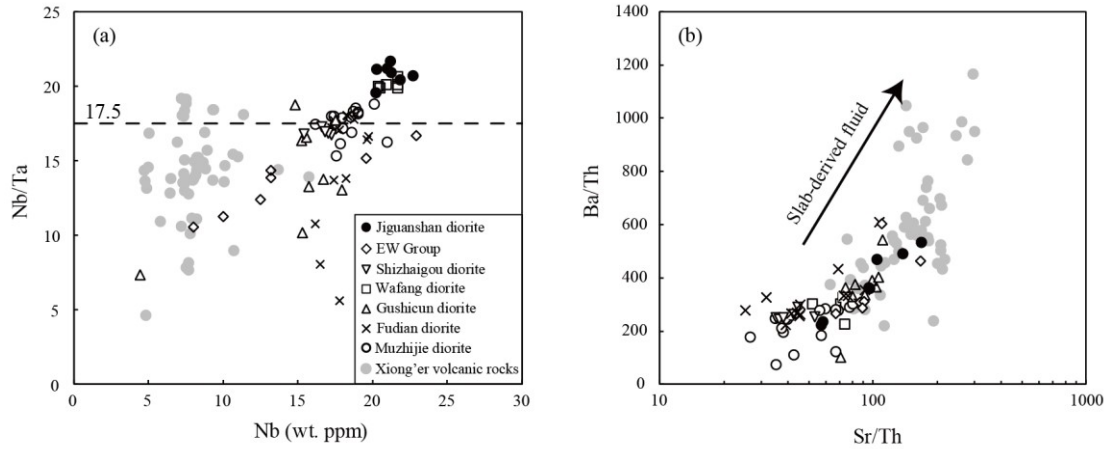
894 **Figure 8** (a) $(^{207}\text{Pb}/^{204}\text{Pb})\text{i}$ versus $(^{206}\text{Pb}/^{204}\text{Pb})\text{i}$; (b) $(^{208}\text{Pb}/^{204}\text{Pb})\text{i}$ versus $(^{206}\text{Pb}/^{204}\text{Pb})\text{i}$. Data for
895 Xiong'er Group from [Zhao \(2000\)](#), for mafic dyke swarms from [Hu et al. \(2010\)](#), [Peng et al.,](#)
896 [\(2007\)](#) and for diorites from [Peng et al. \(2007\)](#), [Wang et al. \(2016\)](#)



897

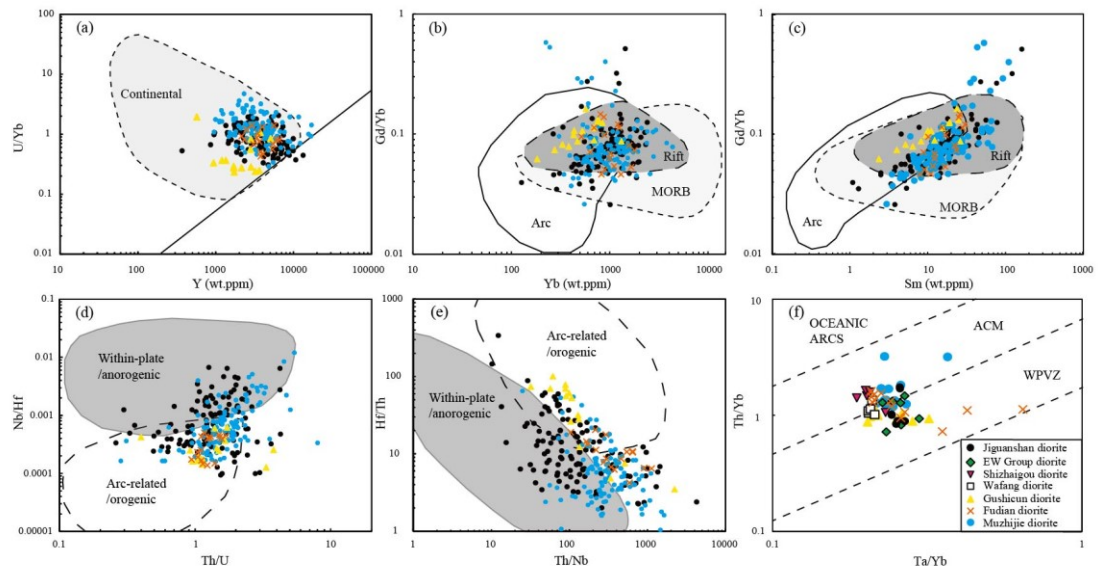
898 **Figure 9** (a) Cr (wt. ppm) content versus MgO content (wt. %); (b) CaO (wt. %) content versus SiO₂
899 content (wt. %); (c) Al₂O₃ (wt. %) content versus SiO₂ content (wt. %); (d) Na₂O (wt. %)
900 content versus SiO₂ content (wt. %); (e) K₂O (wt. %) content versus SiO₂ content (wt. %); (f)

901 TiO_2 (wt. %) content versus SiO_2 content (wt. %); (g) Eu/Eu^* value versus Sr content (ppm);
 902 (h) La/Yb value versus La content (ppm); (i) Zr/Sm value versus Zr content (ppm)



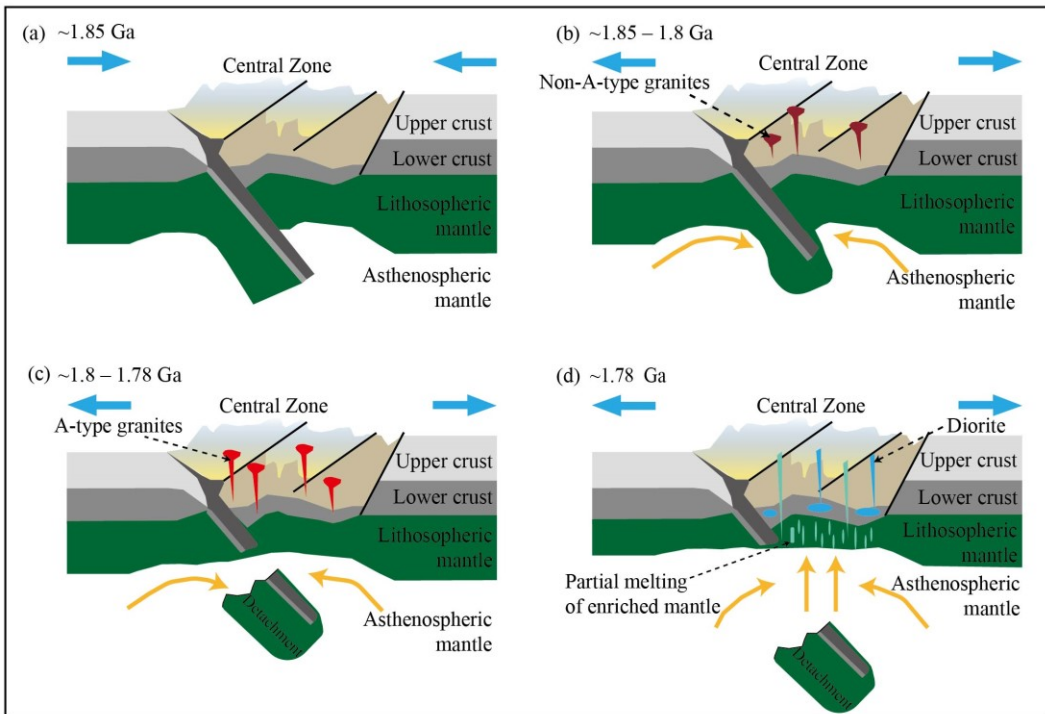
903

904 **Figure 10** (a) Nb/Ta versus Nb content (ppm); (b) Ba/Th value versus Sr/Th values; Data for
 905 Xiong'er Group from [He et al. \(2008, 2010\)](#), [Wang et al. \(2010\)](#), [Zhao et al. \(2002\)](#)



906

907 **Figure 11** (a) Zircon trace element U/Yb ratio versus Y (ppm) (after [Grimes et al., 2007](#)); (b)
 908 Zircon Gd/Yb ratio versus Yb content (ppm) (after [Carley et al., 2014](#)); (c) Zircon Gd/Yb
 909 ratio versus Sm content (ppm) (after [Carley et al., 2014](#)); (d) Zircon Nb/Hf ratio versus Th/U
 910 ratio (after [Hawkesworth and Kemp, 2006](#)); (e) Zircon Hf/Th ratio versus Th/Nb ratio (after
 911 [Yang et al., 2012](#)); (f) Whole-rock trace element Th/Yb ratio versus Ta/Yb ratio (after [Pearce,
 912 1983](#); [Gorton and Schandl, 2000](#))



913

914 **Figure 12** Tectonic evolution in the North China Craton during the Paleoproterozoic (after [Wang](#)
915 [et al., 2004; Deng et al., 2016](#)): (a) ~1.85 Ga: Western and Eastern Blocks collision; (b)
916 ~1.85–1.8 Ga: Post-collisional crustal thickening and granite emplacement; (c) ~1.8–1.78 Ga:
917 Post-collisional delamination and formation of A-type granite; (d) ~1.78 Ga: Transition from
918 post-collisional to rift setting

919

920

921 **Table**922 **Table 1** Major (wt. %) and trace element contents (ppm) of the Jiguanshan diorite

Sample No.	ZY2201	ZY2202	ZY2203	ZY2204	ZY2205	ZY2206	ZY2207
(wt.%)							
SiO ₂	58.18	59.44	59.13	58.24	56.26	56.01	55.57
TiO ₂	1.87	1.37	1.36	1.82	2.01	1.87	2.05
Al ₂ O ₃	14.38	14.37	14.24	14.11	14.18	15.00	14.41
^T Fe ₂ O ₃	10.38	9.04	9.17	10.00	10.35	10.18	10.50
MnO	0.15	0.14	0.14	0.14	0.17	0.14	0.15
MgO	2.73	2.81	2.96	2.59	2.70	2.92	2.94
CaO	5.85	5.29	5.33	5.60	5.61	6.06	5.81
Na ₂ O	2.76	2.85	2.87	2.79	2.56	2.60	2.56
K ₂ O	2.98	3.15	3.16	3.11	3.21	2.97	3.01
P ₂ O ₅	0.71	0.46	0.45	0.65	0.73	0.68	0.76
LOI	0.48	1.31	0.67	0.36	1.53	1.60	1.67
Total	100.47	100.23	99.48	99.41	99.31	100.03	99.43
(ppm)							
Li	11.2	19.8	19.9	14.8	18.6	20.7	18.2
Be	2.66	2.80	2.76	2.94	3.06	2.70	2.97
Sc	22.7	20.1	20.4	23.3	24.3	24.0	23.8
V	163	141	147	168	179	165	164
Cr	72.1	91.3	101.3	69.5	68.6	78.6	83.5
Ni	21.3	22.3	24.0	20.7	19.2	20.2	21.6
Cu	20.8	19.8	19.9	20.9	27.0	22.2	23.3
Zn	131	128	122	133	148	139	141
Ga	21.9	21.9	21.8	22.9	23.3	23.8	22.7
Rb	80.3	95.2	97.8	88.4	88.0	89.5	88.9
Sr	412	374	384	406	403	542	490
Y	47.5	44.4	43.8	48.4	49.3	44.8	46.7
Zr	402	478	474	435	428	400	407
Nb	20.2	21.2	21.0	21.2	22.7	20.3	21.8
Cs	0.60	0.77	0.74	0.95	2.98	3.63	4.44
Ba	1543	1515	1504	1544	1814	1714	1737
La	72.2	79.0	79.5	75.0	77.3	71.7	75.2
Ce	149	161	161	154	163	150	159
Pr	17.6	18.3	18.1	18.2	19.4	18.0	18.9
Nd	72.3	71.2	70.9	73.2	80.0	72.9	77.1
Sm	12.7	12.1	12.0	12.7	14.0	12.8	13.4
Eu	2.63	2.21	2.18	2.59	2.93	2.78	2.87
Gd	12.1	11.2	11.2	12.1	13.0	11.7	12.5

Tb	1.53	1.39	1.40	1.51	1.63	1.47	1.56
Dy	8.99	8.32	8.11	8.92	9.50	8.53	9.00
Ho	1.67	1.54	1.53	1.67	1.75	1.53	1.65
Er	4.97	4.56	4.54	4.95	5.09	4.55	4.87
Tm	0.62	0.55	0.55	0.60	0.63	0.55	0.58
Yb	4.26	3.79	3.84	4.18	4.33	3.82	3.99
Lu	0.61	0.55	0.56	0.60	0.63	0.55	0.58
Hf	7.97	9.09	9.15	8.20	8.46	7.59	7.98
Ta	1.03	0.98	0.99	1.01	1.10	0.96	1.07
Pb	16.4	21.2	18.0	16.3	18.9	15.2	14.2
Th	4.28	6.43	6.71	4.27	3.87	3.22	3.55
U	0.70	0.98	0.88	0.71	0.75	0.61	0.68
K ₂ O/Na ₂ O	1.08	1.11	1.10	1.11	1.25	1.14	1.18
K ₂ O+Na ₂ O (Wt.%)	5.74	6.00	6.03	5.90	5.77	5.57	5.57
Mg#	34.5	38.3	39.2	34.1	34.3	36.5	35.9
A/CNK	0.78	0.81	0.80	0.78	0.79	0.81	0.80
A/NK	1.85	1.77	1.75	1.77	1.84	2.00	1.93
ΣREE	361.5	375.8	375.1	370.4	393.2	361.2	381.3
Eu/Eu*	0.64	0.57	0.57	0.63	0.65	0.68	0.66
(La/Yb) _N	12.2	15.0	14.8	12.9	12.8	13.5	13.5

$$\text{Mg}^{\#} = (\text{MgO} + \text{FeO}_{\text{total}}) / \text{MgO} \times 100$$

Eu/Eu* = 2Eu_N/(Sm_N + Gd_N); (La/Yb)_N = chondrite-normalized La/Yb ratio

923

924

Table 2 Whole-rock Sr isotopic compositions of the late Paleoproterozoic diorites in the NCC

Sample	Age (Ma)	Rb (ppm)	Sr (ppm)	Rb/Sr	$^{87}\text{Rb}/^{86}\text{Sr}$	$^{87}\text{Sr}/^{86}\text{Sr}$	$\pm 2\text{SE}$	$^{87}\text{Sr}/^{86}\text{Sr}$ (t)	Error (abs.)	Data source
Jiguanshan diorite										
ZY2201	1780	80.3	412	0.20	0.5648	0.71931	0.000010	0.70485	0.00077	
ZY2202	1780	95.2	374	0.25	0.7371	0.72471	0.000012	0.70584	0.00099	
ZY2203	1780	97.8	384	0.25	0.7377	0.72434	0.000011	0.70546	0.00099	
ZY2204	1780	88.4	406	0.22	0.6307	0.72111	0.000011	0.70496	0.00085	This study
ZY2205	1780	88.0	403	0.22	0.6334	0.71856	0.000011	0.70235	0.00086	
ZY2206	1780	89.5	542	0.17	0.4780	0.71518	0.000011	0.70294	0.00066	
ZY2207	1780	88.9	490	0.18	0.5252	0.71542	0.000013	0.70198	0.00072	
Wafang diorite										
WF1307-3	1780	107.0	389	0.28	0.7969	0.72131	0.000013	0.70091	0.00106	
WF1307-4	1780	109.0	400	0.27	0.7895	0.72144	0.000014	0.70123	0.00105	
WF1307-5	1780	84.0	411	0.20	0.5921	0.72024	0.000016	0.70508	0.00080	Wang et al. (2016)
WF1307-8	1780	113.0	343	0.33	0.9548	0.72479	0.000016	0.70035	0.00127	
WF1307-9	1780	110.0	373	0.29	0.8545	0.72236	0.000014	0.70048	0.00114	
Shizhaigou diorite										
Ln-1	1780	103.7	272	0.38	1.1040	0.72874	0.000012	0.70048	0.00146	
Ln-2	1780	101.5	322	0.31	0.9125	0.72868	0.000015	0.70532	0.00121	Cui et al. (2011)
Ln-3	1780	136.4	200	0.68	1.9758	0.72509	0.00001	0.67452	0.00259	

Ln-4	1780	116.6	295	0.40	1.1479	0.73149	0.000015	0.70210	0.00152
Ln-5	1780	112.5	300	0.38	1.0885	0.72997	0.000014	0.70211	0.00144
E-W Group dyke									
02SX001	1780	154.8	470	0.33	0.9542	0.72970	0.000014	0.70528	0.00127
02SX007	1780	81.2	450	0.18	0.5231	0.71858	0.000014	0.70519	0.00072
03LF01	1780	74.4	449	0.17	0.4801	0.71619	0.000013	0.70390	0.00066
03FS04	1780	131.8	229	0.58	1.6748	0.74399	0.000012	0.70112	0.00220
03FS07	1780	106.0	539	0.20	0.5699	0.71852	0.000013	0.70393	0.00078
Weight mean value									
						0.70519	0.00031	(n=8, calculated by IsoplotR)	

$$({}^{87}\text{Sr}/{}^{86}\text{Sr})_s = ({}^{87}\text{Sr}/{}^{86}\text{Sr})_0 + ({}^{87}\text{Rb}/{}^{86}\text{Sr})_s \times (e^{\lambda t} - 1)$$

$$\lambda_{87\text{Rb}} = 1.42 \times 10^{-11} \text{ a}^{-1}$$

Error of initial ratio is calculated from the measurement error of the isotope ratio, the estimated concentration error and the age error. The decay constant is considered to be a fixed value.

$\sigma_{\text{Sr}(t)}$ is mean-square deviation of $({}^{87}\text{Sr}/{}^{86}\text{Sr})_t$

σ_{Rb} is mean-square deviation of $({}^{87}\text{Rb}/{}^{86}\text{Sr})_s$

σ_t is mean-square deviation of age

$$\sigma_{\text{Sr}(t)} = \sqrt{\sigma_{\text{Sr}}^2 + \sigma_{\text{Rb}}^2 (e^{\lambda t} - 1)^2 + \sigma_t^2 (\lambda e^{\lambda t} (\frac{{}^{87}\text{Rb}}{{}^{86}\text{Sr}}))^2}$$

Table 3 Whole-rock Nd isotopic compositions of the late Paleoproterozoic diorites in the NCC

Sample	Age (Ma)	Nd (ppm)	Sm (ppm)	$^{147}\text{Sm}/^{144}\text{Nd}$	$^{143}\text{Nd}/^{144}\text{Nd}$	Error (2s)	$^{143}\text{Nd}/^{144}\text{Nd}$	Error (t)	$\varepsilon_{\text{Nd}}(t)$	Error (abs.)	T_{DM2} (εNd)	Data source
Jiguanshan diorite												
ZY2201	1780	72.3	12.7	0.1063	0.511238	0.000007	0.509994	0.000063	-6.69	1.24	2.83	
ZY2202	1780	71.2	12.1	0.1029	0.511129	0.000008	0.509924	0.000061	-8.04	1.20	2.94	
ZY2203	1780	70.9	12.0	0.1022	0.511131	0.000005	0.509934	0.000060	-7.85	1.19	2.93	
ZY2204	1780	73.2	12.7	0.1049	0.511240	0.000007	0.510011	0.000062	-6.35	1.22	2.80	This study
ZY2205	1780	80.0	14.0	0.1058	0.511329	0.000007	0.510090	0.000063	-4.80	1.23	2.68	
ZY2206	1780	72.9	12.8	0.1058	0.511317	0.000005	0.510078	0.000063	-5.03	1.23	2.70	
ZY2207	1780	77.1	13.4	0.1054	0.511320	0.000006	0.510086	0.000062	-4.88	1.22	2.68	
E-W Group dyke												
02SX001	1780	113	20.3	0.1084	0.511287	0.000009	0.510018	0.000065	-6.21	1.27	2.79	
02SX007	1780	62.6	11.3	0.1093	0.511285	0.000010	0.510005	0.000065	-6.47	1.28	2.81	
03LF01	1780	45.1	8.36	0.1120	0.511358	0.000017	0.510047	0.000068	-5.64	1.34	2.75	Peng et al. (2007)
03FS04	1780	102	17.5	0.1039	0.511270	0.000010	0.510053	0.000062	-5.53	1.22	2.74	
03FS07	1780	62.7	11.1	0.1068	0.511297	0.000013	0.510047	0.000064	-5.65	1.26	2.75	
Shizhaigou diorite												
Ln-1	1780	69.0	12.3	0.1075	0.511280	0.000012	0.510021	0.000065	-6.15	1.26	2.79	
Ln-2	1780	66.4	11.7	0.1065	0.511270	0.000011	0.510023	0.000064	-6.10	1.25	2.78	Cui et al. (2011)

Ln-3	1780	61.9	11.2	0.1090	0.511280	0.000011	0.510003	0.000065	-6.50	1.28	2.82
Ln-4	1780	71.1	12.6	0.1072	0.511260	0.000011	0.510005	0.000064	-6.46	1.26	2.81
Ln-5	1780	69.4	12.3	0.1072	0.511260	0.000012	0.510005	0.000064	-6.46	1.26	2.81
Wafang diorote											
WF1307-3	1780	78.4	13.7	0.1056	0.511169	0.000008	0.509953	0.000062	-7.90	1.23	2.93
WF1307-4	1780	78.5	14.1	0.1086	0.511215	0.000008	0.509965	0.000063	-7.67	1.26	2.91
WF1307-5	1780	75.9	13.7	0.1091	0.511192	0.000008	0.509936	0.000064	-8.24	1.27	2.96
WF1307-8	1780	77.6	13.4	0.1044	0.511039	0.000007	0.509837	0.000061	-10.2	1.21	3.11
WF1307-9	1780	77.5	13.9	0.1084	0.511193	0.000005	0.509945	0.000063	-8.07	1.26	2.94
Gushicun diorite											
20XRδ-1	1780	58.0	10.9	0.1134	0.511327	0.000004	0.509999	0.000067	-6.58	1.31	2.82
20XRδ-3	1780	63.3	11.7	0.1118	0.511334	0.000006	0.510025	0.000066	-6.08	1.30	2.78
20XRδ-4	1780	59.1	10.9	0.1118	0.511341	0.000006	0.510032	0.000066	-5.94	1.30	2.77
20XRδ-5	1780	53.1	9.9	0.1122	0.511354	0.000006	0.510041	0.000066	-5.77	1.30	2.76
The Muzhijie diorites											
20δPt2-1	1780	63.5	11.5	0.1090	0.511297	0.000004	0.510021	0.000064	-6.15	1.26	2.79
20δPt2-3	1780	64.2	11.7	0.1100	0.511300	0.000004	0.510012	0.000065	-6.33	1.27	2.80
20δPt2-5	1780	66.4	12.3	0.1122	0.511295	0.000007	0.509982	0.000067	-6.92	1.30	2.85
20δPt2-7	1780	72.1	13.1	0.1101	0.511297	0.000008	0.510007	0.000065	-6.42	1.28	2.81
20δPt2-9	1780	54.2	9.6	0.1076	0.511181	0.000006	0.509922	0.000064	-8.09	1.25	2.95
20δPt2-11	1780	64.5	11.4	0.1073	0.511199	0.000006	0.509943	0.000064	-7.69	1.25	2.91
20δPt2-13	1780	62.9	11.2	0.1076	0.511196	0.000008	0.509937	0.000064	-7.80	1.25	2.92
20δPt2-16	1780	67.9	12.3	0.1098	0.511270	0.000007	0.509984	0.000065	-6.87	1.28	2.85

Fudian diorite

20XRSC-1	1780	65.8	12.1	0.1110	0.511309	0.000006	0.510009	0.000066	-6.39	1.29	2.81	Ma et al. (2023b)
20XRSC-2	1780	67.1	12.3	0.1111	0.511315	0.000006	0.510014	0.000066	-6.30	1.29	2.80	
20XRSC-3	1780	69.5	12.8	0.1113	0.511314	0.000004	0.510011	0.000066	-6.35	1.29	2.80	
20XRSC-4	1780	67.5	12.5	0.1117	0.511311	0.000007	0.510002	0.000066	-6.52	1.30	2.82	
20XRSC-5	1780	70.1	12.9	0.1111	0.511311	0.000006	0.510010	0.000066	-6.37	1.29	2.81	
20XRSC-6	1780	68.9	12.7	0.1112	0.511324	0.000005	0.510022	0.000066	-6.14	1.29	2.79	
20XRSC-8	1780	71.7	12.9	0.1089	0.511331	0.000006	0.510056	0.000065	-5.46	1.26	2.75	
20XRSC-9	1780	76.6	13.9	0.1096	0.511325	0.000005	0.510042	0.000065	-5.74	1.27	2.75	
Weight mean value									-6.51	0.20		(n = 41, calculated by IsoplotR)

$$(^{143}\text{Nd}/^{144}\text{Nd})_s = (^{143}\text{Nd}/^{144}\text{Nd})_0$$

$$+ (^{147}\text{Sm}/^{144}\text{Nd})_s \times (e^{\lambda t} - 1)$$

$$\varepsilon_{\text{Nd}}(t) = [(^{143}\text{Nd}/^{144}\text{Nd})_t / (^{143}\text{Nd}/^{144}\text{Nd})_{\text{CHUR}(t)} - 1] \times 10000$$

$$T_{\text{DM2}} = 1/\lambda \times \ln \{ 1 + [(^{143}\text{Nd}/^{144}\text{Nd})_{\text{DM}} - (^{143}\text{Nd}/^{144}\text{Nd})_s + ((^{147}\text{Sm}/^{144}\text{Nd})_s - (^{147}\text{Sm}/^{144}\text{Nd})_{\text{CC}}) \times (e^{\lambda t} - 1)] / ((^{147}\text{Sm}/^{144}\text{Nd})_{\text{DM}} - (^{147}\text{Sm}/^{144}\text{Nd})_{\text{CC}}) \}$$

$$\lambda_{^{147}\text{Sm}} = 0.654 \times 10^{-11} \text{ a}^{-1}$$

$$^{143}\text{Nd}/^{144}\text{Nd})_{\text{DM}} = 0.51315$$

$$^{147}\text{Sm}/^{144}\text{Nd})_{\text{DM}} = 0.2137$$

$$^{147}\text{Sm}/^{144}\text{Nd})_{\text{CC}} = 0.12$$

Error of initial ratio is calculated from the measurement error of the isotope ratio, the estimated concentration error and the age error. The decay constant is considered to be a fixed value.

$\sigma_{Nd(t)}$ is mean-square deviation of

$(^{143}\text{Nd}/^{144}\text{Nd})_t$

σ_{Sm} is mean-square deviation of

$(^{143}\text{Sm}/^{144}\text{Nd})_s$

σ_t is mean-square deviation of age

$$\sigma_{Nd(t)} = \sqrt{\sigma_{Nd}^2 + \sigma_{Sm}^2 (e^{\lambda t} - 1)^2 + \sigma_t^2 (\lambda e^{\lambda t} (\frac{^{147}\text{Sm}}{^{144}\text{Nd}}))^2}$$

929

930

931 **Table 4** Whole-rock Pb isotopic compositions of the Jiguanshan diorite

Spon.no	U (ppm)	Th (ppm)	Pb (ppm)	$^{206}\text{Pb}/^{204}\text{Pb}$	$\pm 2\text{SE}$	$^{207}\text{Pb}/^{204}\text{Pb}$	$\pm 2\text{SE}$	$^{208}\text{Pb}/^{204}\text{Pb}$	$\pm 2\text{SE}$	$^{206}\text{Pb}/^{204}\text{Pb}$ initial	$^{207}\text{Pb}/^{204}\text{Pb}$ initial	$^{208}\text{Pb}/^{204}\text{Pb}$ initial	$^{238}\text{U}/^{204}\text{Pb}$ μ	$^{232}\text{Th}/^{204}\text{Pb}$	$^{232}\text{Th}/^{238}\text{U}$ ω
ZY2201	0.70	4.28	16.38	15.867	0.0005	15.189	0.0005	36.502	0.0014	15.063	15.103	35.027	2.6	16.0	6.3
ZY2202	0.98	6.43	21.20	16.167	0.0008	15.243	0.0009	37.126	0.0022	15.295	15.150	35.392	2.8	18.8	6.8
ZY2203	0.88	6.71	18.03	15.882	0.0006	15.182	0.0006	36.494	0.0013	14.965	15.084	34.398	2.9	22.8	7.8
ZY2204	0.71	4.27	16.29	16.097	0.0010	15.225	0.0009	37.324	0.0023	15.271	15.137	35.825	2.6	16.3	6.2
ZY2205	0.75	3.87	18.90	15.832	0.0007	15.179	0.0006	36.046	0.0016	15.095	15.100	34.901	2.3	12.4	5.3
ZY2206	0.61	3.22	15.22	15.914	0.0010	15.170	0.0010	36.124	0.0024	15.164	15.090	34.939	2.4	12.9	5.4
ZY2207	0.68	3.55	14.22	16.036	0.0008	15.199	0.0007	36.338	0.0016	15.136	15.103	34.931	2.9	15.3	5.4

Initial Pb isotopic ratios are calculated back to
1780 Ma.

932

933

934 **Table S captions**

935 **Table S1** Zircon U–Pb isotopic data for the Jiguanshan diorite obtained by the LA-ICP-MS
936 technique

937 **Table S2** Zircon trace element data for the Jiguanshan diorite obtained by the LA-ICP-MS
938 technique

939

940